



HAL
open science

Filtering and segmentation of 3D angiographic data: Advances based on mathematical morphology

Alice Dufour, Olena Tankyevych, Benoît Naegel, Hugues Talbot, Christian Ronse, Joseph Baruthio, Petr Dokládál, Nicolas Passat

► **To cite this version:**

Alice Dufour, Olena Tankyevych, Benoît Naegel, Hugues Talbot, Christian Ronse, et al.. Filtering and segmentation of 3D angiographic data: Advances based on mathematical morphology. *Medical Image Analysis*, 2013, 17 (2), pp.147-164. 10.1016/j.media.2012.08.004 . hal-01719012

HAL Id: hal-01719012

<https://hal.univ-reims.fr/hal-01719012v1>

Submitted on 27 Feb 2018

HAL is a multi-disciplinary open access archive for the deposit and dissemination of scientific research documents, whether they are published or not. The documents may come from teaching and research institutions in France or abroad, or from public or private research centers.

L'archive ouverte pluridisciplinaire **HAL**, est destinée au dépôt et à la diffusion de documents scientifiques de niveau recherche, publiés ou non, émanant des établissements d'enseignement et de recherche français ou étrangers, des laboratoires publics ou privés.

Filtering and segmentation of 3D angiographic data: Advances based on mathematical morphology

Alice Dufour, Olena Tankyevych, Benoît Naegel, Hugues Talbot, Christian Ronse, Joseph Baruthio, Petr Dokládál, Nicolas Passat

► **To cite this version:**

Alice Dufour, Olena Tankyevych, Benoît Naegel, Hugues Talbot, Christian Ronse, et al.. Filtering and segmentation of 3D angiographic data: Advances based on mathematical morphology. Medical Image Analysis, Elsevier, 2013, 17 (2), pp.147-164. <10.1016/j.media.2012.08.004>. <hal-00679008>

HAL Id: hal-00679008

<https://hal.archives-ouvertes.fr/hal-00679008>

Submitted on 14 Mar 2012

HAL is a multi-disciplinary open access archive for the deposit and dissemination of scientific research documents, whether they are published or not. The documents may come from teaching and research institutions in France or abroad, or from public or private research centers.

L'archive ouverte pluridisciplinaire **HAL**, est destinée au dépôt et à la diffusion de documents scientifiques de niveau recherche, publiés ou non, émanant des établissements d'enseignement et de recherche français ou étrangers, des laboratoires publics ou privés.

Filtering and segmentation of 3D angiographic data: Advances based on mathematical morphology

O. Tankyevych^(a), A. Dufour^{(b,c)*}, B. Naegel^(b), H. Talbot^(d), C. Ronse^(a),
J. Baruthio^(b), P. Dokládal^(e) and N. Passat^(b)

^(a) Université Paris-Est Créteil, LISSI, EA 3956, France

^(b) Université de Strasbourg, LSIT, UMR CNRS 7005, France

^(c) Université de Strasbourg, LINC, UMR CNRS 7237, France

^(d) Université Paris-Est, LIGM, UMR 8049 CNRS, France

^(e) Mines ParisTech, CMM, Fontainebleau, France

Abstract

In the last 20 years, 3D angiographic imaging proved its usefulness in the context of various clinical applications. However, angiographic images are generally difficult to analyse due to their size and the fact that useful information is easily hidden in noise and artifacts. Therefore, there is an ongoing necessity to provide tools facilitating their visualization and analysis, while vessel segmentation from such images remains a challenging task. This article presents new vessel segmentation and filtering techniques, relying on recent advances in mathematical morphology. In particular, methodological results related to variant mathematical morphology and connected filtering are stated, and involved in an angiographic data processing framework. These filtering and segmentation methods are validated on real and synthetic 3D angiographic data.

1 Introduction

The important rise of medical imaging during the 20th century, mainly induced by physics breakthroughs related to nuclear magnetic resonance and X-rays, has led to the development of imaging modalities devoted to visualize vascular structures. The analysis of such angiographic images is of great interest for several clinical applications. Initially designed to generate 2D data, these imaging modalities progressively led to the acquisition of 3D images, enabling the visualization of vascular volumes.

However, such 3D data are generally quite large, being composed of several millions of voxels, while the useful vascular information generally represents less than 5% of the whole volume. In addition to this sparseness, the frequent low signal-to-noise ratio and the potential presence of artifacts (due to acquisition, patient movements, etc.) make the analysis of such images a challenging task. In order to assist the users of such data (radiologists, clinicians, etc.), it is therefore necessary to design software tools enabling them to visualize as well as possible the relevant information embedded in these images.

One of the main ways to perform such a task is to develop filtering and/or segmentation methods, *i.e.*, routines which enhance or extract the vessels from angiographic images. In particular, such methods are required to be as ergonomic as possible, for instance by providing user-friendly and time-saving interactive *modus operandi*.

Recently, several methodological works have been conducted in the field of mathematical morphology. Some of them, and especially those related to spatially variant mathematical morphology and connected filtering, can be efficiently

*The research leading to these results has been partially funded by a PhD grant of the *Région Alsace* (France) and the *Centre National de la Recherche Scientifique* (CNRS, France).

involved in the design of relevant tools for vessel filtering and segmentation from 3D angiographic data, especially Computed Tomography Angiography (CTA) and Magnetic Resonance Angiography (MRA). This article aims at presenting some of these new mathematical morphology concepts, and their applicative use in this complex field of medical image processing.

The remainder of this article is organized as follows. Section 2 proposes a synthetic state of the art related to mathematical morphology in medical image processing (Section 2.1), and vessel segmentation from 3D angiographic data (Section 2.2). Section 3 provides useful definitions and notations. The next two sections gather the main contributions of this article. Section 4, which is an extended and improved version of the conference articles [71, 70], describes a vessel filtering method based on a hybrid strategy, merging both new spatially variant mathematical morphology algorithms and derivative-based approaches. Section 5, which is an extended and improved version of the conference articles [56, 19], describes an example-based interactive vessel segmentation method relying on a component-tree-based technique. Section 6 describes and discusses experimental results related to vessel segmentation and filtering performed on angiographic phantom images and *in vivo* cerebral MRA data. Concluding remarks emphasizing contributions and remaining challenges are proposed in Section 7.

2 State of the art

2.1 Mathematical morphology in medical imaging

Mathematical morphology is a well-established theory of non-linear, order-based image analysis [51]. It relies on basic operations (namely erosions, dilations, openings, closings), involving geometric patterns (structuring elements, or SEs for brief). These low-level SE-based operations made it possible to design the first image processing segmentation methods (*e.g.*, for 2D vessel segmentation [73]), and remained further frequently used for several purposes (*e.g.*, for 2D [83] and 3D vessel segmentation [13], or for skull stripping [16]).

Based on these basic mathematical morphology operations, higher-level image processing techniques were developed and used in the context of medical image processing. Watersheds [78] were indeed considered for 3D vessel segmentation [58], 3D vertebrae labelling [46], 4D heart segmentation [14], or 3D brain structure segmentation from newborn brain MRI [25]. The grey-level hit-or-miss transform [48] was also considered, essentially in the field of 3D vessel segmentation [49, 6]. Finally, connected filters [65] and especially those based on component-trees (described in Section 5.2) were involved in several (bio)medical applications, including 3D vessel filtering and segmentation [80, 76, 9], 3D brain structures segmentation [17], and 2D melanocytic nevi segmentation [47].

The use of mathematical morphology in these techniques was, in particular, motivated by the ability of the involved operators to efficiently integrate and model *a priori* knowledge enabling an efficient detection of the structures of interest with a wide range of using policies (automated, semi-automated, knowledge-based and/or interactive ones).

2.2 Filtering and segmentation of 3D angiographic data

Filtering and segmentation of vascular structures (generally from MR and CT angiography) has been an active research field since the end of the 80's (see, *e.g.*, [20, 31] for pioneering works). These intensive efforts were motivated by the possible use of such segmentation results, *e.g.*, for pathology detection and quantification, or for surgical planning. A complete state of the art is beyond the scope of this article. The reader will find up-to-date surveys on 3D angiographic segmentation in [36, 72].

Most of the main image processing and analysis concepts have been involved in the development of 3D vessel segmentation methods. Non-exhaustively, one can cite: region-growing [74], deformable models [41, 15], statistical analysis [12, 62], minimal path-finding [37], vessel tracking [22, 43], differential analysis [66], or mathematical morphology (discussed in Section 2.1). Despite this wide range of methodological contributions, the results provided by segmentation methods generally remain perfectible. The handling of under-segmentation (*e.g.*, in the case of small vessels, of signal decrease, or of partial volume effect) and over-segmentation (*e.g.*, in the case of neighbouring with other anatomical structures, or of high intensity artifacts), the robustness to image degradations (low signal-to-noise ratio), the low computational cost, the guarantee of termination and convergence, are indeed desirable properties that are not often satisfied.

Consequently, a reasonable trend over the last few years has been to cross methodologies. Indeed, hybrid vessel segmentation methods present a range of possible solutions for overcoming certain weaknesses of each method and combining their advantages. One of the most popular hybrid strategies is based on the combination of multi-scale differential analysis with deformable models, such as level-sets [10], B-spline snakes [23]) and maximum geometric flow [3]. Deformable methods with energy minimizing functionals have also been combined with statistical region-based information in a multi-scale feature space [27]. Tracking strategies were reinforced by gradient flux of circular cross-sections in [35], while in [24] multiple hypothesis tracking were used with Gaussian vessel profile and statistical model fitting. In [81], a probabilistic method for axis finding was proposed within a minimal path finding strategy. Note finally that mathematical morphology has also been used with other techniques, for instance in [32] where watersheds and neural networks were combined, and in [69], where multi-scale morphology was used together with Gabor wavelets.

An alternative way to improve vessel segmentation efficiency consists of injecting high-level guiding knowledge in the segmentation process. This can be achieved by designing vascular atlases devoted to explicitly guide segmentation tools [60, 59]. Also, instead of using atlases, it may be possible to use segmentation examples, thus leading to the design of example-based segmentation processes. A last strategy is to directly take advantage of users skills in order to guide the segmentation process, thus leading to interactive methods. This last strategy however requires the interaction to be both easy to carry out and quick, since medical experts generally cannot afford to spend much time with segmentation tasks.

These considerations motivate, in particular, the new filtering and segmentation methods described in the next sections. Indeed, in Section 4, a hybrid strategy, mixing differential analysis and mathematical morphology is proposed for 3D vessel filtering. In Section 5, an interactive and example-based segmentation method, relying on connected filtering, is described. These two methods take advantage of recent methodological advances in mathematical morphology. We show that they can also be conveniently fused, leading to improved results.

3 Notations

Let $E = \prod_{i=1}^3 \llbracket 0, d-1 \rrbracket$ (with $d \in \mathbb{N}^*$) be a subset of \mathbb{Z}^3 . The set E provides a (discrete) model for the part of \mathbb{R}^3 where will be defined the considered 3D images. An element of E (called point, or voxel), is noted $x = (x_1, x_2, x_3)$.

Let $V = \llbracket \perp, \top \rrbracket$ (with $\perp < \top \in \mathbb{Z}$) be a subset of \mathbb{Z} . The set V provides a (discrete) model for the value space of the considered 3D images. An element of V (called value, or grey level), is noted v .

A (grey-level) image I is defined as a function

$$\left| \begin{array}{l} I : E \rightarrow V \\ x \mapsto v \end{array} \right. \quad (1)$$

and we note $I : E \rightarrow V$ or $I \in V^E$. The set E is called the support of I . By abuse of notation, a (binary) image $B : E \rightarrow \{0, 1\}$ will also be considered as the set $B^{-1}(\{1\}) = \{x \in E \mid B(x) = 1\}$.

The thresholding function at value $v \in V$ is defined by

$$\left| \begin{array}{l} \lambda_v : V^E \rightarrow 2^E \\ I \mapsto \{x \in E \mid v \leq I(x)\} \end{array} \right. \quad (2)$$

The cylinder function of support $X \subseteq E$ and of value $v \in V$ is defined by

$$\left| \begin{array}{l} C_{X,v} : E \rightarrow V \\ x \mapsto \begin{cases} v & \text{if } x \in X \\ \perp & \text{otherwise} \end{cases} \end{array} \right. \quad (3)$$

The impulse function at point $p \in E$ and of value $v \in V$ is defined by

$$\left| \begin{array}{l} i_{p,v} : E \rightarrow V \\ x \mapsto \begin{cases} v & \text{if } x = p \\ \perp & \text{otherwise} \end{cases} \end{array} \right. \quad (4)$$

In particular, we have $i_{p,v} = C_{\{p\},v}$.

4 Vessel filtering: a morpHo-Hessian approach

4.1 Motivation

3D angiographic imaging modalities (*e.g.*, MRA, CTA) can provide a detailed visualization of vascular networks up to the resolution of the generated data. However, the small size and complexity of the vascular structures, coupled to noise, acquisition artifacts, and blood signal heterogeneity (especially signal discontinuity) make the analysis of such data a hard task, thus justifying intensive efforts devoted, in particular, to filtering (*i.e.*, vessel enhancement).

Vessel filtering has often been considered *via* the use of Gaussian second derivative analysis, and more especially Hessian matrix analysis. This approach enables the detection of thin objects and their principal directions, at possibly different scales. Compared with first derivative (*i.e.*, gradient) approaches, the Hessian matrix can also capture some shape characteristics. In particular, the eigenvalues of the Hessian matrix can be combined into *vesselness* functions in order to discriminate such shapes [40, 66, 23], 34].

An alternative to these linear approaches is proposed by spatially variant mathematical morphology (SVMM) [4, 5]. The algorithms defined in this framework are formulated with the purpose of filtering images in a way which depends on the location in the dataset [44, 77, 18]. Such filtering techniques can provide some solutions in order to reduce noise and possibly reconnect vessels despite signal decrease/loss, by taking advantage of local shape knowledge.

In this section, we propose a hybrid filtering method devoted to 3D angiographic image analysis. This method especially aims to retrieve the smallest (low-intensity) vessels and correctly reconnect them. Based on Hessian analysis, the local orientation of the vessels is first sought. A spatially-variant morphological closing according to these local orientations is then performed.

The combination of linear and non-linear techniques is motivated by several facts. The Hessian analysis is robust and fast for object direction detection as well as multiple scales, whereas orientation analysis using purely mathematical morphology methods would require directional sampling, which would be prohibitive in 3D. Conversely, for reconnection and noise reduction, anisotropic diffusion, that has been previously used together with Hessian analysis, *e.g.*, in [42], requires several iterations and is subject to convergence issues, while a spatially-variant closing or opening converges in a single iteration.

4.2 Background notions: Hessian-based analysis

One of the main challenges in image analysis is to design operators that are translation, rotation and scale-invariant. Translation invariance is satisfied by all convolution kernels, by definition. Rotation invariance can be guaranteed either by using rotation-invariant kernels or when the preferred direction is fixed relatively to the image. Scale invariance can be satisfied by derivatives of Gaussian filters. Linear combinations of derivatives of Gaussian filter kernels constitute, in particular, the basic feature detectors within linear scale-space theory [38].

The Hessian matrix \mathcal{H} is obtained from the Gaussian second derivative analysis of a 3D image F at each voxel in the six principal directions

$$\mathcal{H} = \begin{bmatrix} \frac{\partial^2 F}{\partial x_1^2} & \frac{\partial^2 F}{\partial x_1 \partial x_2} & \frac{\partial^2 F}{\partial x_1 \partial x_3} \\ \frac{\partial^2 F}{\partial x_2 \partial x_1} & \frac{\partial^2 F}{\partial x_2^2} & \frac{\partial^2 F}{\partial x_2 \partial x_3} \\ \frac{\partial^2 F}{\partial x_3 \partial x_1} & \frac{\partial^2 F}{\partial x_3 \partial x_2} & \frac{\partial^2 F}{\partial x_3^2} \end{bmatrix} \quad (5)$$

This Hessian matrix \mathcal{H} can be decomposed into three eigenvalues, λ_1 , λ_2 and λ_3 (with $|\lambda_1| \leq |\lambda_2| \leq |\lambda_3|$) associated to three eigenvectors \mathbf{e}_1 , \mathbf{e}_2 and \mathbf{e}_3 . When λ_1 is close to zero and much smaller than λ_2 and λ_3 , the locally characterized shape is a linear (bright) structure, *e.g.*, a vessel in angiographic data. Its orientation is then given by \mathbf{e}_1 (\mathbf{e}_2 and \mathbf{e}_3 then form a basis for the plane orthogonal to the linear bright structure).

When appropriately designed and applied at multiple scales, combinations of the three eigenvalues, often called *vesselness* function, should give the strongest response at one particular scale corresponding to the plate-, blob-like and/or tubular objects [66, 23]. Hereafter, and in the remainder of this article, we consider the vesselness function proposed in [23]) (which has been experimentally assessed as the most robust in the current applicative context). For a 3D grey-level

image, observed at a point x , and a scale σ (directly linked to the standard deviation of the considered Gaussian kernel), this vesselness function ν is formulated as follows

$$\nu(x, \sigma) = \begin{cases} 0 & \text{if } \lambda_2 > 0 \text{ or } \lambda_3 > 0 \\ (1 - \exp(\frac{-R_A^2}{2\alpha^2})) \cdot \exp(-\frac{R_B^2}{2\beta^2}) \cdot (1 - \exp(\frac{-S^2}{2c^2})) & \text{otherwise} \end{cases} \quad (6)$$

with

$$\begin{cases} R_A = \frac{|\lambda_2|}{|\lambda_3|} \\ R_B = \frac{|\lambda_1|}{\sqrt{|\lambda_2 \lambda_3|}} \\ S = \sqrt{\sum_{j=1}^3 \lambda_j^2} \end{cases} \quad (7)$$

where R_A differentiates between planar and line-like objects, R_B differentiates blob-like ones, and S accounts for the intensity difference between objects and background. The parameters α , β and c influence the sensitivity of the filter to the corresponding measures.

As stated in Equation (6), the filter can be applied at different scales, which can provide results in a large range of object sizes. After normalization, the maximal vesselness value is selected for each point x . The corresponding scale then provides an estimate of the object width.

4.3 Background notions: (Spatially variant) mathematical morphology

We now introduce some notions of mathematical morphology and spatially variant mathematical morphology.

Definition 1 (Adjunction) Let \mathcal{L} and \mathcal{M} be two complete lattices (a complete lattice is a partially ordered set (X, \leq) , such that every subset S of X has an infimum in X denoted $\bigwedge S$, and a supremum in X denoted $\bigvee S$). Two operators $\delta : \mathcal{L} \rightarrow \mathcal{M}$ and $\varepsilon : \mathcal{M} \rightarrow \mathcal{L}$ form an adjunction (ε, δ) if and only if for all $x \in \mathcal{L}$ and all $y \in \mathcal{M}$, we have

$$\delta(x) \leq y \Leftrightarrow x \leq \varepsilon(y) \quad (8)$$

From these notions, it is then possible to introduce the basic operators of morphology, namely, dilation, erosion, opening and closing.

Definition 2 (Erosions, dilations, openings and closings) With the same hypotheses as in Definition 1, the operator δ commutes with the supremum operator \bigvee and is called a dilation, while the operator ε commutes with the infimum operator \bigwedge and is called an erosion. Moreover, the operator $\gamma = \delta\varepsilon$ is called an opening, and the operator $\varphi = \varepsilon\delta$ is called a closing.

We have the following general properties of openings and closings.

Property 3 Let \mathcal{L} and \mathcal{M} be two complete lattices. Let γ and φ be the opening and closing induced by an adjunction for \mathcal{L}, \mathcal{M} . Let $x \in \mathcal{L}$ and $y \in \mathcal{M}$. Then we have:

$$\text{(Idempotence)} \quad \begin{cases} \gamma\gamma = \gamma \\ \varphi\varphi = \varphi \end{cases} \quad (9)$$

$$\text{(Increasingness)} \quad x \leq y \Rightarrow \begin{cases} \gamma(x) \leq \gamma(y) \\ \varphi(x) \leq \varphi(y) \end{cases} \quad (10)$$

$$\text{((Anti-)extensivity)} \quad \begin{cases} x \leq \varphi(x) \\ \gamma(x) \leq x \end{cases} \quad (11)$$

These properties are useful from both algebraic and practical points of view. Indeed, the behaviour of morphological operators is well defined. It is therefore possible to design new operators (e.g., gradients, top-hats) exploiting differences between these operators.

We now assume that $\mathcal{L} = \mathcal{M}$. In the ‘‘grey-level’’ case (e.g., in flat morphology [26]), \mathcal{L} is the family of grey-level images V^E equipped with the point-wise partial order on functions \leq . Let $B \subseteq E$ be a binary set, also called *structuring element* (SE). Let $\delta_B, \varepsilon_B : V^E \rightarrow V^E$ be the dilation and the erosion induced by B . The dilation of the impulse function $i_{p,v}$ (with $p \in E$ and $v \in V$) is defined as $\delta_B(i_{p,v}) = C_{B_p,v}$, with $B_p = \{x + p \mid x \in B\}$. From this expression, we derive the classical definitions of the dilation and erosion for a function $f : E \rightarrow V$

$$\delta_B(f)(x) = \bigvee_{p \in B} f(x - p) = \bigvee_{p \in \check{B}_x} f(p) \quad (12)$$

$$\varepsilon_B(f)(x) = \bigwedge_{p \in B} f(x + p) = \bigwedge_{p \in B_x} f(p) \quad (13)$$

where $\check{B} = \{-p \mid p \in B\}$ is the *transpose* of B .

In the (more general) case of SVMM, the involved SE B is often denoted as *structuring function* and is actually defined as $B : E \rightarrow 2^E$. Consequently, $B(x)$ is the structuring element considered at point $x \in E$. The *transpose* of a structuring function B , still noted $\check{B} : E \rightarrow 2^E$, is now defined, for all $x \in E$ by

$$\check{B}(x) = \{y \in E \mid x \in B(y)\} \quad (14)$$

Here, the dilation of the impulse function $i_{p,v}$ is defined as $\delta_B(i_{p,v}) = C_{B(p),v}$. From this expression, we derive the spatially-variant definition of the dilation and erosion for a function $f : E \rightarrow V$

$$\delta_B(f)(x) = \bigvee_{p \in \check{B}(x)} f(p) \quad (15)$$

$$\varepsilon_B(f)(x) = \bigwedge_{p \in B(x)} f(p) \quad (16)$$

With the definitions given above, the standard and SV morphological erosion and dilation form an adjunction. Then, we can define, in both cases, the morphological opening and closing, as

$$\gamma_B = \delta_B \varepsilon_B \quad (17)$$

$$\varphi_B = \varepsilon_B \delta_B \quad (18)$$

The transpose \check{B} of B is used in Equation (15) for the computation of δ_B . In addition to being computationally expensive, it can, under some conditions, be of larger extent than any of the B function, although if the family of B is bounded, so is \check{B} . This may become computationally problematic for implementing filters based on adjunctions of dilations and erosions in order to compute a closing or an opening. However, by considering the (equivalent) alternative following formulation of Equation (15)

$$\delta_B(f) = \bigvee_{p \in E} C_{B(p),f(p)} \quad (19)$$

it turns out that the computation of $\delta_B(f)$ can be performed independently of \check{B} , then leading to the following result.

Proposition 4 *The SV dilation and the SV adjunct erosion can be computed with the same algorithmic cost $\mathcal{O}(MN)$ where $N = |E|$, and $M = \mathcal{O}(\max_{x \in E}\{|B(x)|\})$.*

4.4 Methodology

In this section, we describe a vessel filtering methodology, with a focus on the detection of small vessels and their correct reconnection. This morpho-Hessian filter performs like a reconnecting inverse diffusion filter, in some ways. It first distinguishes the vessel-like objects and their local orientation. Then, it performs a spatially-variant morphological closing (assuming that vessels are bright structures on a dark background) according to these local directions.

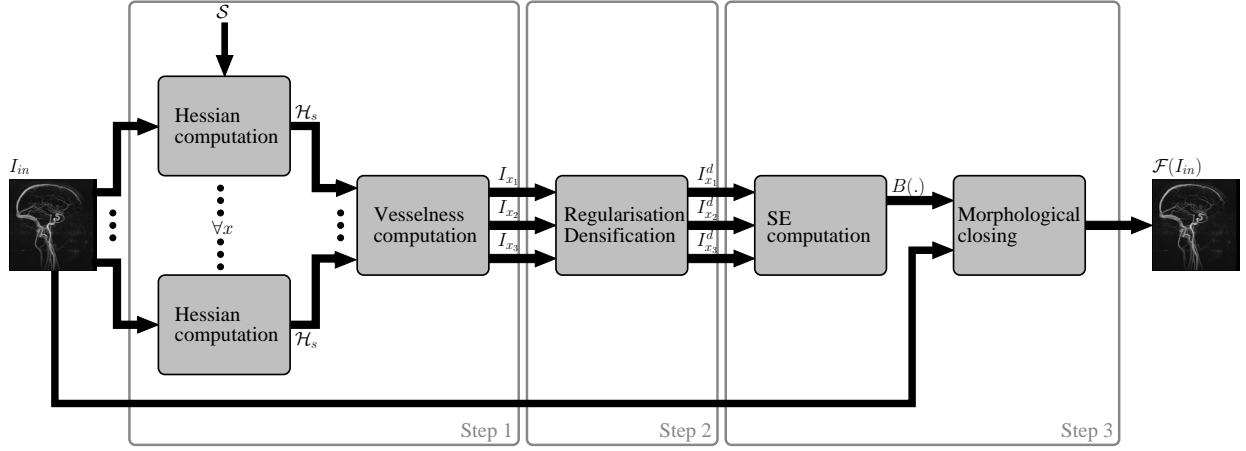


Figure 1: Visual outline of the filtering method described in Section 4.4. Step 1: vessel detection (see Section 4.4.2). Step 2: directional field correction (see Section 4.4.3). Step 3: vessel reconnection (see Section 4.4.4).

4.4.1 Outline of the method

The method takes as input:

- a 3D grey-level angiographic image $I_{in} : E \rightarrow V$, e.g., a MRA or CTA image.

The proposed filter is fully automatic. It is however parametric, in order to allow the user to choose the size of the vessels to detect, and the gap length between vessels to reconnect. The process, visually summarized in Figure 1, is divided into three main steps:

1. the Hessian matrix of I_{in} is computed for each point of E at different scales, resulting into a vesselness image I_{ves} and leading to define three images corresponding to the principal vessel directions: I_{x_1} , I_{x_2} and I_{x_3} (see Section 4.4.2);
2. from a thresholded version of I_{ves} and the direction images I_{x_1} , I_{x_2} , I_{x_3} , and with the help of morphological thinning and dilation, dense and regular vessel direction fields $I_{x_1}^d$, $I_{x_2}^d$ and $I_{x_3}^d$ are obtained (see Section 4.4.3);
3. a family of structuring elements, composed of segments of fixed length, oriented with respect to $I_{x_1}^d$, $I_{x_2}^d$ and $I_{x_3}^d$, is involved in an SV morphological closing operation carried out on I_{in} (see Section 4.4.4).

The method finally provides as output:

- a 3D grey-level filtered image $\mathcal{F}(I_{in}) : E \rightarrow V$ of the input image I_{in} , such that $I_{in} \leq \mathcal{F}(I_{in})$ (i.e., $I_{in}(x) \leq \mathcal{F}(I_{in})(x)$ for any $x \in E$), and enabling in particular to reconnect high intensity linear structures of I_{in} .

4.4.2 Step 1: vessel detection

Given a set of different scales \mathcal{S} enabling to characterize vessels among different radii, the image I_{in} is first convolved with a Gaussian kernel $G(x, s) = (2\pi s^2)^{-N/2} \cdot \exp(-\frac{|x|^2}{2s^2})$ at each scale $s \in \mathcal{S}$. For each point $x \in E$, its Hessian matrix \mathcal{H}_s is then computed. The eigen form of this matrix, i.e.,

$$\mathcal{H}_s = \begin{bmatrix} \lambda_1 & 0 & 0 \\ 0 & \lambda_2 & 0 \\ 0 & 0 & \lambda_3 \end{bmatrix} \quad (20)$$

enables the computation of a score in x from the vesselness function defined in Equation (6). The maximal score among the scales of \mathcal{S} is chosen for each point x as its best response $\nu_{max}(x) = \max_{s \in \mathcal{S}} \{\nu(x, s)\}$.

The associated basis vectors ($\mathbf{e}_1, \mathbf{e}_2, \mathbf{e}_3$) (forming the basis of the eigen form of \mathcal{H}_s) are assumed to define the orientation of the characterized shape in x . In particular, the vectors \mathbf{e}_1 are stored in three images as the principal directions (along the principal axes): $I_{x_1}, I_{x_2}, I_{x_3} : E \rightarrow [-1, 1]$, defined, for all $x \in E$, by

$$\mathbf{e}_1(x) = I_{x_1}(x) \cdot \mathbf{e}_{x_1} + I_{x_2}(x) \cdot \mathbf{e}_{x_2} + I_{x_3}(x) \cdot \mathbf{e}_{x_3} \quad (21)$$

where $(\mathbf{e}_{x_1}, \mathbf{e}_{x_2}, \mathbf{e}_{x_3})$ is the canonical basis of \mathbb{R}^3 .

4.4.3 Step 2: directional field correction

In order to propagate objects outside their own boundary with the spatially-variant morphological closing (or, in fact, with many other filtering methods as well), it is necessary to have a *dense* direction vector field. In our case, the directional information is necessary only as far as the dilation can reach. One could use the gradient vector flow [82] or an average square gradient within a diffusion scheme to obtain a dense direction field as in [77].

On the other hand, the directions obtained by second-order derivatives can get chaotic at the end of tubular object segments, which might cause problems in methods that use them in further procedures. For this, a *regularized* direction vector field is highly desirable. Here, in order to obtain both dense and regularized direction field, we have come up with a procedure based on several simple morphological operations.

At first, as the expression of vesselness (see Equation (6)) expresses the probability of being a vessel for each point (thus varying between 0 and 1), the vesselness image I_{ves} is thresholded so that most of the vessel-like objects are preserved. By using the thresholded vesselness result I_{ves}^t , we make sure that we use the tubular objects as markers for direction field propagation. Then, we perform a binary morphological thinning of the direction field (I_{x_1}, I_{x_2} and I_{x_3}) guided by the thresholded vesselness result I_{ves}^t with a structuring element of fixed size. After follows the adjunct dilation –still solely of the direction field– guided by the thresholded vesselness result. This results into dense and regularized direction fields $I_{x_1}^d, I_{x_2}^d$ and $I_{x_3}^d$. A schematic representation of the operation is illustrated in Figure 2.

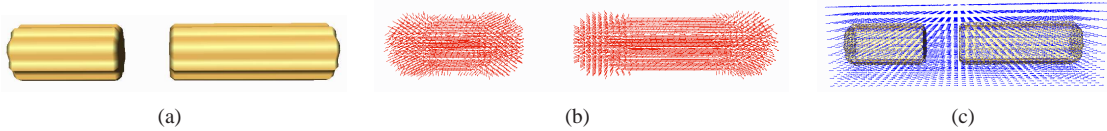


Figure 2: Vector field regularization. (a) Original broken cylinder. (b) Direction field of the thresholded vesselness of the cylinder. (c) Regularized direction field guided by the thresholded vesselness (blue) and original object (yellow).

4.4.4 Step 3: vessel reconnection

In this last step, an SV morphological closing operation is performed over the image I_{in} with the aim of reconnecting vessels. First, a morphological dilation is applied with a structuring function $B : E \rightarrow 2^E$ (see Section 4.3), providing, for each $x \in E$, a structuring element $B(x)$ centred on x , of fixed length, and oriented according to $\mathbf{e}_1(x)$. The (discrete) direction \mathbf{e}_1 of $B(x)$ is approximated from the images of regularized direction fields, $I_{x_1}^d, I_{x_2}^d$ and $I_{x_3}^d$, by defining a discrete (Bresenham) segment.

The SE-based adjunct dilation, resulting in the image $\delta_B(I_{in})$, is followed by the adjunct erosion ε_B . Both computations (δ_B and ε_B), whose results are formally defined by Equations (19) and (16) respectively, then provide the final filtering result $\mathcal{F}(I_{in}) = \varphi_B(I_{in})$ with a low algorithmic cost (see Proposition 4). Also note that this processing ensures idempotence, guaranteeing that the filter obeys morphological rules. This methodology is validated in Section 6.

5 Interactive vessel segmentation: a component-tree based approach

5.1 Motivation

Most 3D vessel segmentation techniques are designed to be globally automated (except, sometimes, for initialization and/or termination, or for the determination of parameters). Automation is generally justified by the difficulty for medical experts to spend too much time for guiding such segmentation methods. The counterpart of this fact is that such automatic methods do not take much advantage of the user's expertise (*e.g.*, clinician, radiologist, etc.), thus leading to possible segmentation errors (in addition to a frequently high computational cost).

The recent rise of interactive segmentation in several application fields can modify this conception of vessel segmentation [45]. Indeed, by opposition to standard automatic segmentation, interactive segmentation strongly relies on the user's skills. In particular, the user must generally initialize the process, by providing (background and/or object) markers which strongly influence the results (for instance in the case of watersheds [78], graph-cuts [7] or binary partition tree algorithms [63]). Interaction also implies such methods to be very efficient (especially in terms of computational cost).

Such guidance may be potentially time consuming for the user, especially in the case of 3D images. However, a compromise between automatic and interactive segmentation could be proposed, based on the concept of example-based segmentation, which has been considered in several application fields before being applied to medical imaging [21]. Indeed, the use of segmentation examples may lead to an automatic presegmentation of the image, which may constitute the object markers.

The *component-tree* is a graph-based structure which models some characteristics of a grey-level image by considering its binary level-sets obtained from successive thresholding operations (see, *e.g.*, [51], Chapter 7). It has been involved, in particular, in the development of morphological operators [8, 64], and used for designing segmentation procedures in several medical applications (see Section 2.1).

By definition, component-trees are particularly well-suited for the design of methods devoted to process and/or analyse grey-level images based on *a priori* hypotheses related to the topology (connectedness) and the specific intensity (locally/globally minimal or maximal) of structures of interest. It has to be noticed that several works related to component-trees have been devoted to enable their efficient computation [64, 50, 79]. In particular, the ability to compute component-trees in quasi-linear time opens the way to the development of interactive and efficient segmentation methods.

Based on recent theoretical developments [56] related to interactive segmentation based on component-trees, we propose in the sequel a segmentation method that combines the advantages of example-based segmentation in terms of automation (since it avoids manual marker positioning or presegmentation by the user) and the ability to take into account the skills of the user in a quite simple and intuitive fashion. Indeed the only interaction consists of a thresholding process, which only requires a few seconds.

5.2 Background notions (component-trees)

Let us consider a given connectivity on \mathbb{Z}^3 , for instance the standard 6- or 26-connectivity [33] (in the sequel of this section, some alternative morphological connectivities will also be considered). For a given binary image B defined on E , we denote by $\mathcal{C}[B]$ the set of the connected components (*i.e.*, the maximal connected sets) of B with respect to this connectivity. Note that a grey-level image $I \in V^E$ can be expressed as

$$I = \bigvee_{v \in V} \bigvee_{X \in \mathcal{C}[\lambda_v(I)]} C_{X,v} \quad (22)$$

Let $\mathcal{K} = \bigcup_{v \in V} \mathcal{C}[\lambda_v(I)]$ be the set of the connected components generated by the thresholdings of I at all values $v \in V$. The Hasse diagram of the partially ordered set (\mathcal{K}, \subseteq) is a tree (*i.e.*, a connected acyclic graph), and more especially a rooted tree, the root of which is the supremum $\lambda_{\perp}(I) = E$. This tree is called the *component-tree* of I .

Definition 5 (Component-tree) Let $I \in V^E$ be a grey-level image. The component-tree of I is the rooted tree $T =$

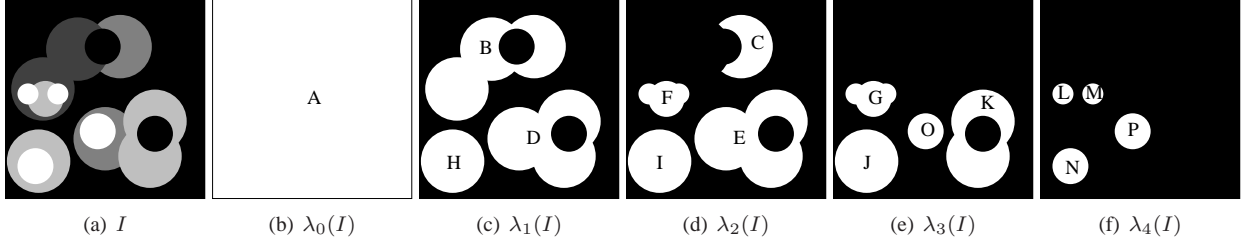


Figure 3: (a) A grey-level image $I : E \rightarrow V = \llbracket 0, 4 \rrbracket$ (from 0, in black, to 4, in white). (b–f) Threshold images $\lambda_v(I)$ (in white) for v varying from 0 (b) to 4 (f).

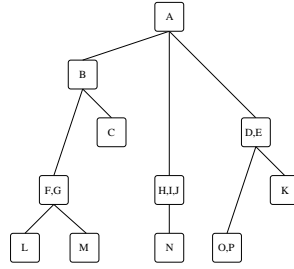


Figure 4: The component-tree T of I (see Figure 3(a)). The letters (A–R) in nodes correspond to the associated connected components in Figure 3(b–f).

(\mathcal{K}, L, R) such that:

$$\mathcal{K} = \bigcup_{v \in V} \mathcal{C}[\lambda_v(I)] \quad (23)$$

$$L = \{(X, Y) \in \mathcal{K}^2 \mid Y \subset X \wedge \forall Z \in \mathcal{K}, Y \subseteq Z \subset X \Rightarrow Y = Z\} \quad (24)$$

$$R = \text{sup}(\mathcal{K}, \subseteq) = X_{\perp}(I) = E \quad (25)$$

The elements of \mathcal{K} (resp. of L) are the nodes (resp. the (oriented) edges) of T . The node R is the root of T . For any $N \in \mathcal{K}$, we set $ch(N) = \{N' \in \mathcal{K} \mid (N, N') \in L\}$; $ch(N)$ is the set of the children of N .

An example of component-tree defined for a 2D image is illustrated on Figures 3 and 4. Component-trees can be used to develop image processing/analysis procedures based on filtering or segmentation strategies [30]. Such procedures generally consist of determining a subset $\hat{\mathcal{K}} \subseteq \mathcal{K}$ among the nodes of the component-tree $T = (\mathcal{K}, L, R)$ of a considered image $I : E \rightarrow V$.

When performing segmentation, the (binary) resulting image $B \subseteq E$ is defined as the union of the nodes of $\hat{\mathcal{K}}$, i.e., as

$$B = \bigcup_{X \in \hat{\mathcal{K}}} X \quad (26)$$

In this context, determining the nodes to be preserved is a complex issue, which can be handled by considering attributes [75] (i.e., qualitative or quantitative information related to each node) to characterize the nodes of interest. An alternative solution, based on an example-based paradigm, can also be considered. This strategy is described below.

5.3 Theory

A way to consider the previously enunciated segmentation problem is to search the set of nodes $\hat{\mathcal{K}} \subseteq \mathcal{K}$ which generates a binary object being as similar as possible to a given approximate precomputed segmentation. This issue can be formalized

as the resolution of the following optimization problem

$$\widehat{\mathcal{K}} = \arg \min_{\mathcal{K}' \subseteq \mathcal{K}} \left\{ d \left(\bigcup_{N \in \mathcal{K}'} N, M \right) \right\} \quad (27)$$

where $M \subseteq E$ is the (binary) approximate segmentation, and d is a measure on 2^E . An intuitive solution for determining a useful measure is to consider the amount of false positives/negatives induced by $X = \bigcup_{N \in \mathcal{K}'} N$ with respect to M

$$d^\alpha(X, M) = \alpha \cdot |X \setminus M| + (1 - \alpha) \cdot |M \setminus X| \quad (28)$$

where $\alpha \in [0, 1]$ controls the trade-off between the tolerance to false positives and false negatives.

The function \mathcal{F}^α proposed hereafter enables to build a binary image whose connected components form a set $\widehat{\mathcal{K}}$ which is a solution of Equation (27).

Proposition 6 ([56]) *Let $\alpha \in [0, 1]$. Let $I \in V^E$. Let $T = (\mathcal{K}, L, R)$ be the component-tree of I . Let $M \subseteq E$. Let $\mathcal{F}^\alpha : \mathcal{K} \rightarrow 2^{\mathcal{K}}$ and $c^\alpha : \mathcal{K} \rightarrow \mathbb{R}^+$ be the functions recursively cross-defined, for all $N \in \mathcal{K}$, by*

$$\mathcal{F}^\alpha(N) = \begin{cases} \{N\} & \text{if } \alpha \cdot n(N, M) < (1 - \alpha) \cdot p^*(N, M) + \sum_{N' \in \text{ch}(N)} c^\alpha(N') \\ \bigcup_{N' \in \text{ch}(N)} \mathcal{F}^\alpha(N') & \text{otherwise} \end{cases} \quad (29)$$

and

$$c^\alpha(N) = \begin{cases} \alpha \cdot n(N, M) & \text{if } \alpha \cdot n(N, M) < (1 - \alpha) \cdot p^*(N, M) + \sum_{N' \in \text{ch}(N)} c^\alpha(N') \\ (1 - \alpha) \cdot p^*(N, M) + \sum_{N' \in \text{ch}(N)} c^\alpha(N') & \text{otherwise} \end{cases} \quad (30)$$

where $p^*(N, M) = |(N \setminus \bigcup_{N' \in \text{ch}(N)} N') \cap M|$, and $n(N, M) = |N \setminus M|$. Let $M^\alpha = \bigcup_{N \in \mathcal{F}^\alpha(E)} N$. Then, we have

$$d^\alpha(M^\alpha, M) = c^\alpha(E) = \min_{\mathcal{K}' \subseteq \mathcal{K}} \left\{ d^\alpha \left(\bigcup_{N \in \mathcal{K}'} N, M \right) \right\} \quad (31)$$

It has to be noticed that such a solution can be computed in linear time.

Proposition 7 ([56]) $\mathcal{F}^\alpha(E) = \mathcal{C}[M^\alpha]$ (and thus M^α) can be computed with the linear algorithmic complexity $\mathcal{O}(\max\{|\mathcal{K}|, |E|\})$.

Moreover, the increasing property of thresholding is actually inherited by the developed method.

Proposition 8 ([57]) *Let $I \in V^E$ be a grey-level image. Let $M \subseteq E$. Let $\alpha_1 < \alpha_2 \in [0, 1]$. Then we have $M^{\alpha_2} \subseteq M^{\alpha_1}$.*

Remark 9 *A consequence of this property is the ability to store $k > 2$ different results obtained for k increasing values $0 \leq \alpha_1 < \alpha_2 < \dots < \alpha_{k-1} < \alpha_k \leq 1$, as a grey-level image $S_k : E \rightarrow \llbracket 1, k \rrbracket$ defined, similarly to Equation (22), by*

$$S_k = \bigvee_{i=1}^k C_{M^{\alpha_i}, i} \quad (32)$$

where $M^{\alpha_i} \subseteq E$ is the binary result of the segmentation method for the parameter α_i . In such a situation, we can avoid to store k distinct binary images, and the interactive choice of the result by the user can be made (in real-time) by actually performing a standard thresholding of S_k among the values $\llbracket 1, k \rrbracket$.

5.4 Methodology

In this section, we focus on the description of a methodology for vessel segmentation by means of an example. This method is automated in the first part of its process, and only requires user interaction once a set of binary results has been precomputed and stored in a grey-level image. The interactive part of the method is, in particular, a single thresholding step where the user can tune a parameter controlling the trade-off between false positives and false negatives between the segmentation example and the expected result.

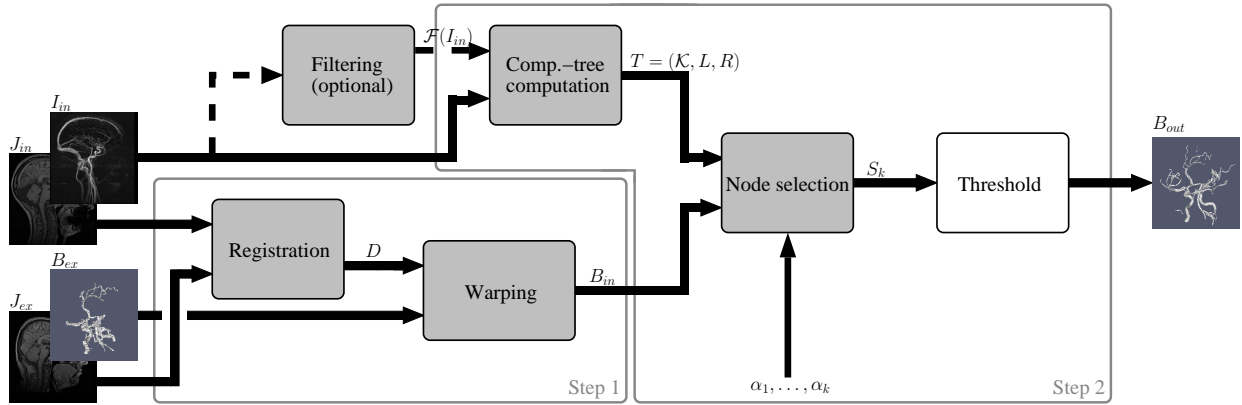


Figure 5: Visual outline of the segmentation method described in Section 5.4. Step 1: example fitting (see Section 5.4.2). Step 2: interactive segmentation (see Section 5.4.3). Grey boxes: automatic steps; white box: interactive step. Continuous arrows: standard workflow; dash arrow: optional supplementary step (filtering, see Sections 4.4 and 5.5, and Figure 1).

5.4.1 Outline of the method

The method takes as input:

- a 3D grey-level angiographic image $I_{in} : E \rightarrow V$, e.g., a MRA or CTA image;
- a 3D vessel segmentation example consisting of a binary image $B_{ex} \subseteq E$ of vascular structures similar to those present in I_{in} , and the grey-level image $I_{ex} : E \rightarrow V$ from which this segmentation has been obtained.

(In Section 5.4.2, it will be observed that it may be also required to provide images $J_{in}, J_{ex} : E \rightarrow V$ for visualizing the morphological structures neighbouring the vessels visualized in I_{in}, I_{ex} .) The only parameter is a threshold value $\alpha \in [0, 1]$ (see Section 5.3), which has to be tuned by the user at the end of the segmentation. The process, visually summarized in Figure 5, is divided into two main steps:

- the first one consists of fitting the binary image B_{ex} onto the image I_{in} using to a registration procedure (see Section 5.4.2);
- once B_{ex} is correctly positioned, the second step mainly consists of the interactive α -tuned segmentation process described in Section 5.3 (see Section 5.4.3).

The method finally provides as output:

- the 3D binary vessel segmentation $B_{out} \subseteq E$, associated to I_{in} , and induced by the example I_{ex} and the chosen parameter α .

5.4.2 Step 1: example fitting

Fitting the binary example B_{ex} onto I_{in} requires a registration/warping process to be performed. Registration of vascular images is a complex task. Indeed, while registration algorithms have arguably reached a satisfactory degree of efficiency for the processing of *dense* images, such as morphological cerebral data [28], the development of efficient registration procedures in the case of *sparse* –and specifically angiographic– data seems to remain a globally open question, despite few recent works [2, 29, 68]. This is *a fortiori* the case for interpatient registration (it is indeed infrequent that I_{in} and I_{ex} are images of a same patient).

Consequently, except in the cases where the angiographic images contain (a sufficient amount of) morphological information, which can happen sometimes for certain angiographic data (e.g., phase-contrast or time-of-flight MRA,

depending on the acquisition parameters), it may be necessary to associate to each angiographic data, namely I_{in} and I_{ex} , a corresponding morphological profile of the same patient (*e.g.*, a T1 MRI data). Since it is quite frequent in clinical practice to acquire such data during an angiographic image acquisition, thus providing couples of morphological/angiographic data (I_{in}, J_{in}) , (I_{ex}, J_{ex}) , such a requirement is actually not a real difficulty.

Under these conditions, registration algorithms devoted to morphological images (see, *e.g.*, [52]) can be involved in the current step. These algorithms consist of determining a deformation field $D : E \rightarrow E$ such that the composition of D and I_{ex} is “semantically” equal to I_{in} , or, more formally, that for all $x \in E$, we have

$$I_{in}(x) \simeq (I_{ex} \circ D^{-1})(x) \quad (33)$$

Such registration procedures can be based on more or less accurate strategies, leading to either rigid, affine, or nonrigid deformation fields D .

Once D is computed from the angiographic data I_{in} and I_{ex} (or, more frequently, from the morphological ones J_{in} and J_{ex}), which can be done in an automatic fashion, the segmentation example B_{ex} remains to be fitted onto the vascular image I_{in} to be segmented. This is actually equivalent to computing the binary image $B_{in} \subseteq E$ as

$$B_{in} = D(B_{ex}) = \{D(x) \mid x \in B_{ex}\}$$

Such a warping procedure can be performed by a simple interpolation step (in order to retrieve a binary result), or by more sophisticated techniques, enabling in particular to preserve structural properties of the segmentation example, as proposed, *e.g.*, in [21].

5.4.3 Step 2: interactive segmentation

Once B_{in} has been computed, it becomes possible to perform a segmentation of I_{in} , guided both by the example B_{in} (which provides an approximate result of the structures of interest in I_{in}), and by the user (who may adjust this approximate result to more accurately fit the semantics of I_{in}).

In the proposed methodological framework, this task is based on the approach developed in Section 5.3 (the “approximate segmentation” M defined in this section actually corresponds to the example B_{in} considered here). In particular, once the component-tree $T = (\mathcal{K}, L, R)$ of I_{in} is computed, the purpose is to determine the set of nodes $\widehat{\mathcal{K}} \subseteq \mathcal{K}$ defined in Equation (27), *i.e.*, the set of binary connected components which leads to the best possible segmentation (M^α , in Section 5.3, which corresponds to B_{out} , here) with respect to the chosen measure d^α controlling the trade-off of false positives/negatives between this solution M^α/B_{out} and the example M/B_{ex} (see Equation (28)).

Practically, as stated in Remark 9, it is necessary to compute several segmentation results for distinct values of the parameter α , leading to a grey-level image (see Equation (32)), the level-sets of which (obtained by a simple user-defined threshold) will finally lead to the final segmentation B_{out} . Note that an alternative solution to this precomputation strategy may be to compute on-the-flight the results successively obtained for different values of α chosen by the user (see Section 7).

5.5 Mask-based connectivity

As stated at the beginning of Section 5.2, the connectivities considered when computing the component-tree of I_{in} are generally the “standard” ones, *i.e.*, those induced by the well-known notions of 6- or 26-adjacency.

A (morphological) alternative definition for connectivity has been proposed with the notion of *second-generation* connectivity [61, 67]. In this context, *mask-based* connectivity [54] proposes to use some (grey-level) mask functions in order to characterize the connected sets. In the binary case, and by only considering masks which are supersets of an image, we derive from [54] the following definition.

Definition 10 (Mask-based connectivity) *Let $X \subseteq E$ be a binary image. Let $\omega(X) \supseteq X$ be a mask of X . The ω -connected components of X , noted $C_\omega[X]$, are the sets $X \cap Y$, for any connected component Y of $\omega(X)$.*

In the sequel, for a given (grey-level) image $I : E \rightarrow V$, we consider extensive masks $\Omega(I) : E \rightarrow V$, *i.e.*, such that $I \leq \Omega(I)$. We call Ω -connected components of I the set of all the ω -connected components of $\lambda_v(I)$ induced by the masks $\omega(\lambda_v(I)) = \lambda_v(\Omega(I))$, at all values $v \in V$. Typical examples of masks verifying these properties are those induced by:

- (flat) dilations, *e.g.*, $I, \delta(I), \dots, \delta^k(I), \dots$;
- (flat) closings, *e.g.*, $I, (\epsilon \circ \delta)(I), \dots, (\epsilon^k \circ \delta^k)(I), \dots$;

with a (well-chosen) structuring element, avoiding in particular translation effects.

It is, of course, possible to build the component-tree of I_{in} induced by the Ω -connected components of the successive level-sets of I [55]. Note in particular that each element of the set \mathcal{K}_Ω of the Ω -connected components of I_{in} will be composed of one or several connected components of I . More precisely, the component-tree and the (Ω -connected) component-tree of I_{in} induce a (surjective) morphism between (\mathcal{K}, \subseteq) and $(\mathcal{K}_\Omega, \subseteq)$.

Broadly speaking, mask-based connectivity involving such extensive masks makes it possible to symbolically reconnect structures which are physically disconnected in I_{in} . In particular, by considering as mask the filtered image $\mathcal{F}(I_{in})$, computed with the method proposed in Section 4, which presents all the required properties, and corrects the disconnection effects resulting from noise, artifacts and/or signal loss, it may be possible to develop an improved version of the segmentation method proposed above. Such an improved version may simply consist of computing B_{out} from B_{ex} and I_{in} equipped with the connectivity provided by the filtered mask $\mathcal{F}(I_{in})$. This strategy is experimentally assessed in the next section.

6 Experiments and results

This section describes experiments carried out to assess the behaviour of the proposed two methods. The filtering method described in Section 4 is validated in Section 6.1 from a quantitative point of view, on synthetic images, and from a qualitative point of view on samples of 3D (MR) angiographic data. The segmentation method described in Section 5 is validated in Section 6.2, on 3D (MR) angiographic data from qualitative and/or quantitative points of view, depending on the assessed criteria, and on the available ground-truths.

6.1 Vessel filtering

We first assess the filtering method described in Section 4. This is done in the context of vessel reconnection in 3D angiographic data. By opposition to the case of vessel segmentation (see Section 6.2), quantitative validations are hardly tractable on real data. Some qualitative (*i.e.*, visual) validations are provided on few 3D samples of real data (same TOF MRAs as those used below, for segmentation experiments), at the end of this section. However, most of the validations presented hereafter, and in particular the quantitative ones, are performed on the synthetic dataset considered in [1].

This dataset is based on a $100 \times 100 \times 100$ isotropic image visualizing a tortuous, branching vessel-like object of varying radii (0.5 to 4 voxels), which does not simulate a specific anatomical structure. The object contained in this image is depicted in Figure 6(a). A slice of the corresponding 3D grey-level image (at different levels of noise) is provided in Figure 6(b–e). The object cross-section intensities present a parabolic profile, ranging from 150 at the object borders, to 200 at its medial axes, while the background intensity is 100, which corresponds to a standard (intensity) model for MRAs, in small vessels neighbourhoods.

In addition to the discrete sampling of the continuous object, which generates errors (due, *e.g.*, to partial volume effects), a Gaussian noise is added to the data, with different standard deviations, namely $\sigma = 10, 20, 40$ and 80 , in the considered images (see Figure 6(b–e)). Note that $\sigma = 20$ globally corresponds to the expected noise in MR or CT data, while $\sigma = 40$ is closer to the noise expected in ultrasound data. The standard deviation $\sigma = 80$ has been considered to explore the limits of the method in the worst cases which may sometimes happen in clinical applications.

These experiments aim at estimating the efficiency of the filtering methodology, and in particular the cost of the reconnections in terms of supplementary noise. This is done in a quantitative fashion in Section 6.1.1, and in a more visual (and then subjective) fashion in Section 6.1.2.

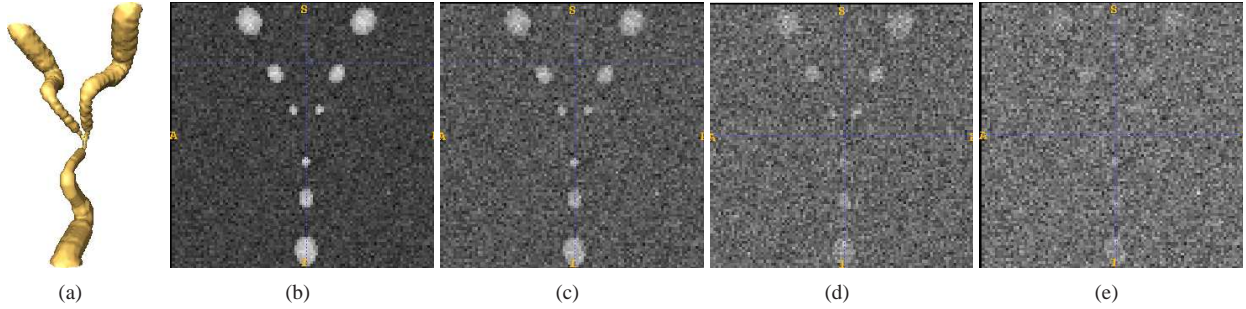


Figure 6: (a) Synthetic 3D object [1] used for validations in Section 6.1. (b–e) Slices of the grey-level image for various levels of additive white Gaussian noise: (b) $\sigma = 10$, (c) $\sigma = 20$, (d) $\sigma = 40$, and (e) $\sigma = 80$.

6.1.1 Experiments on synthetic data

In order to carry out these first validations, we consider the four 3D images $I_\sigma : E \rightarrow V$, namely I_{10} , I_{20} , I_{40} , and I_{80} , illustrated in Figure 6(b–e), where σ is the standard deviation of the Gaussian noise in the image I_σ . Let $G \subseteq E$ be the object visualized in this image, viewed as a binary (ground-truth) object for I_σ .

When performing a thresholding of I_σ at a given value $v \in V$, we obtain a binary (segmented) result $\lambda_v(I) \subseteq E$ which (more or less accurately) approximates G . From a quantitative point of view, this approximation can be expressed in terms of true positives ($G \cap \lambda_v(I)$) and false positives ($\lambda_v(I) \setminus G$).

For experiments, parameters of vesselness were set to $\alpha = \beta = 0.25$ and $\gamma = 5$. We performed a multi-scale Hessian analysis with scales $\sigma \in [1, 4]$ in geometric progression with 5 steps.

We first consider the global quality of the filtering, in terms of proportions of false positives/negatives induced by a subsequent thresholding operation. These are visualized on ROC curves, allowing for a comparison of the proposed filtering with (i) the thresholding of the non-filtered image; (ii) the thresholding of a Hessian-based vesselness function [23]; and (iii) the thresholding of the image filtered by anisotropic diffusion [42]. The four induced ROC curves are computed and compared for the four levels of noise $\sigma = 10, 20, 40$ and 80 . The results of these experiments are shown on Figure 7.

The main purpose of the proposed morpho-Hessian filtering method is its ability to reconnect vessel-like structures. The presence of noise in I_σ may lead to a disconnection of the segmented object $\lambda_v(I)$ into several connected components, especially where the radius of the object becomes close to 0. On the other hand, while reconnecting objects is desirable, it is also an inverse operation that may lead to connecting noise to the main object. In order to assess the “cost” of these reconnections in terms of supplementary noise, for each one of the images previously considered (namely the non-filtered image, vesselness function, anisotropic diffusion image, and morpho-Hessian filtered image), we show the first high accuracy reconnection on each ROC curve corresponding to threshold value of the segmented image $\lambda_v(I_\sigma)$. In other words, these points correspond to the best accuracy result for which the main object is still connected. These reconnection points are depicted by triangular dots in Figure 7.

In the case of lower noise levels, *i.e.*, $\sigma = 10$ and 20 , the proposed morpho-Hessian filter exhibits similar results compared to the original image and anisotropic diffusion filter, while Frangi vesselness is the least accurate. This means the morpho-Hessian filter does not degrade image quality in these cases. For higher levels of noise, the morpho-Hessian filter exhibits better (for $\sigma = 40$) or slightly better results (for $\sigma = 80$) than the original image or anisotropic diffusion filter. However, for the highest level of noise, *i.e.*, $\sigma = 80$ (which is infrequent in clinical practice), the best performance is achieved by Frangi vesselness. In this final case, it seems to be better not to use inverse filtering at all, unless prior filtering is applied.

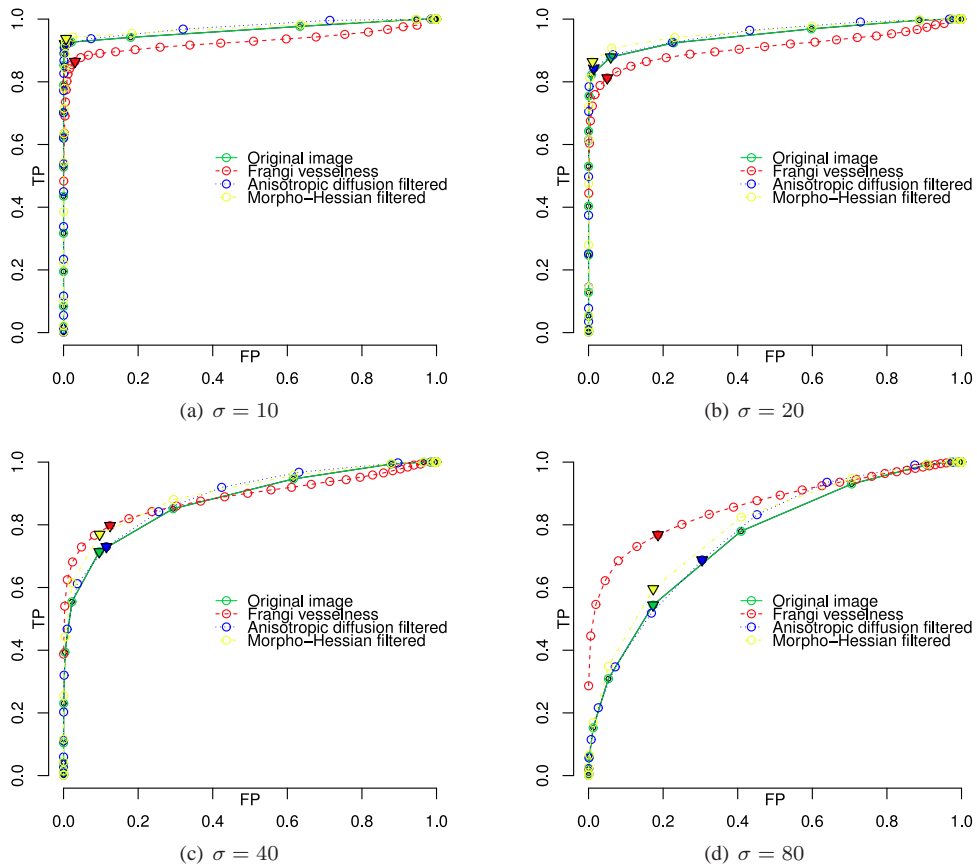


Figure 7: ROC curves of thresholding operations performed on the image I_σ , on its Hessian-based vesselness function, on the image obtained by anisotropic diffusion of I_σ , and on the image $\mathcal{F}(I_\sigma)$ obtained by multiscale morpho-Hessian filtering. The triangular dot on each curve indicates the point at which a correct reconnection of the segmented structure has been obtained. Results for different levels of noise: (a) $\sigma = 10$, (b) $\sigma = 20$, (c) $\sigma = 40$, (d) $\sigma = 80$.

6.1.2 Experiments on real data

In order to conclude this first part of the validations devoted to the proposed morpho-Hessian filtering method, we now consider a few examples obtained from real images. The samples depicted in Figure 8(a,d,g) show maximum intensity projections (MIP) of 3D angiographic data (namely TOF images) altered by signal heterogeneity, resulting in visible disconnections. The corresponding morpho-Hessian filtered images associated to these data are depicted (still in MIP) in Figure 8(b,e,h). In these examples, noise was reduced by morphological openings after applying the morpho-Hessian filter for the sake of visualization.

Qualitatively, these results confirm expectations derived from the synthetic data, namely that the morpho-Hessian filter reconnects vessel without amplifying noise significantly, in medium-noise data. However, it also introduces some undesirable effects, *e.g.*, in Figure 8(b) the red arrow points to a vessel presenting irregular border artifacts. This effect is due to the initial discrete representation of the object combined with scale detection errors. Since both very small vessels and vessel boundaries are sensitive to discretization, in spite of earlier filtering it can still happen that directions are estimated incorrectly near large vessel boundaries. However in practice this effect is observed to be of limited extent.

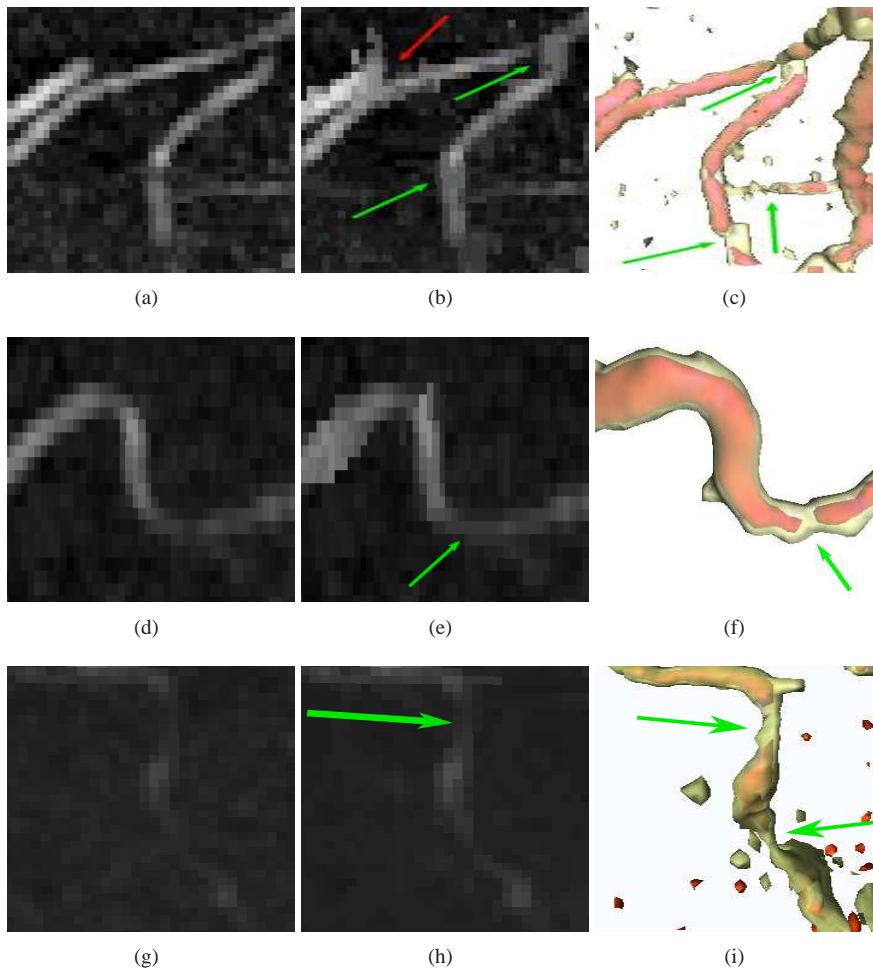


Figure 8: Morpho-Hessian filtering results on real images. (a,d,g) MIP images of (samples of) 3D TOF data. (b,e,h) MIP result of the morpho-Hessian filter. (c,f,i) 3D isosurface rendering of the morpho-Hessian filter (in yellow) superimposed over the initial image (in red). Green arrows indicate some areas of reconnection and red arrows indicate some undesirable effects (see text).

6.2 Vessel segmentation

We now assess the segmentation method described in Section 5. This is done in the context of artery segmentation from 3D angiographic data, namely phase contrast (PC) MRAs (10 images) and time of flight (TOF) MRAs (2 images), of the brain. For each angiographic image, a morphological image of the patient (acquired during the same acquisition) is also considered for registration purpose (a PC MRA magnitude image in the case of PC MRAs, and a T1 MRI in the case of TOF MRAs).

Some examples of images of the considered datasets are illustrated in Figure 9. One can observe that these data are of distinct resolutions (millimetric for PC MRAs, and half-millimetric for TOF MRAs) and of varying quality (low SNR for PC MRAs, and higher SNR for TOF MRAs, all data being without contrast agent injection). Also note that some data visualize both veins and arteries (PC MRAs, with a better contrast on venous structures), or essentially arteries (TOF MRAs, where veins are visible but with a quite lower intensity).

These experiments aim at estimating the global efficiency of the methodology, but also the influence of some key-

elements of the technique, such as registration accuracy, example accuracy, interpatient anatomical variability, and effects of connectivity policies. As in Section 6.1, these experiments are assessed from both quantitative and qualitative (*i.e.*, visual) points of view. This is justified by the fact that realistic example-based segmentation cannot be performed on phantoms, while not much ground-truth is available for MRA data¹.

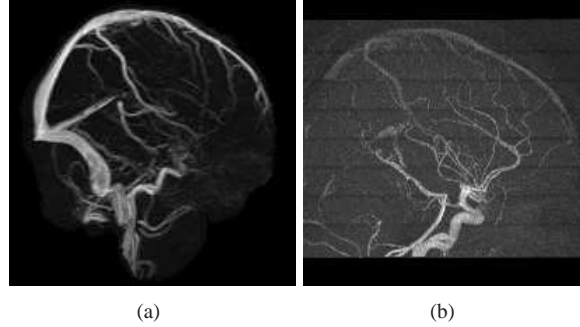


Figure 9: Examples of data considered for vessel segmentation (maximal intensity projection, sagittal plane). (a) Phase contrast MRA (resolution: 1.0mm, no contrast agent injection). (b) Time of flight MRA (resolution: 0.5mm, no contrast agent injection).

6.2.1 Evaluation of the component-tree approach

These first experiments are aimed to assess the relevance of the example-based interactive approach, *i.e.*, to validate the segmentation theory exposed in Section 5.3. In order to do so, we consider an experimental context where neither the registration nor the example quality may affect the results. This can be done by focusing on intra-patient and intra-image experiments.

Practically, for a given MRA image, for which a ground-truth segmentation is available, we perform the example-based interactive segmentation by using, as example, this same ground-truth. This is actually done for one (low resolution, low SNR) PC MRA, and two (high resolution, high SNR) TOF MRA.

Ideally, one may retrieve as result the ground-truth involved as examples. This (expected) correlation is expressed here by using the standard measures of sensitivity (Sen) and positive predictive value (PPV)

$$Sen = \frac{tp}{tp + fn} \quad \text{and} \quad PPV = \frac{tp}{tp + fp} \quad (34)$$

where tp , fp , and fn are the true positives, false positives and false negatives, respectively. Due to the “one-dimensional” nature of the small vessels, which may bias the relevance of these volumic-based measures, both sensitivity and positive predictive values are computed on the 3D results (“3D Sen ” and “3D PPV ”) and on the skeletonized ones (“1D Sen ” and “1D PPV ”). These results are summarized in Table 1, and partially illustrated in Figure 10(a,d).

They tend to show the correct behaviour of the method in case of correct and well positioned example. Note that the results are less satisfactory for low resolution images. This is shown here for PC #1, but also note that the 1D measures are higher than the 3D ones, emphasizing the ability of the method to correctly detect the structure of the vessels, despite possible volumic errors. Also note that some of the ground-truth data are sometimes incomplete (see, *e.g.*, the red parts of Figure 10(d)) which may lead to lower quality measures as should be expected.

It may also be noticed that the use of an example to guide the segmentation process allows users to select specific structures of interest among a set of homogeneous ones, for instance here, arteries among the whole arteriovenous network.

¹Note, moreover, that the use of vascular ground-truth, and in particular manual segmentations performed by experts, is neither a necessary nor a sufficient condition to guarantee the correctness of validations. See, *e.g.*, [9], where some of the authors point out the significant variability in inter-experts segmentation results, which strongly bias the quantitative measures provided by standard criteria.

Table 1: Sensitivity and positive predictive value measures for experiments of Section 6.2.1 (see text). The α value is the one for which the best segmentation has been obtained.

Image	α	3D		1D	
		<i>Sen</i>	<i>PPV</i>	<i>Sen</i>	<i>PPV</i>
TOF #1	0.970	99.99	99.27	99.77	99.79
TOF #2	0.995	100.00	100.00	100.00	100.00
PC #1	0.940	65.77	86.31	82.76	92.70

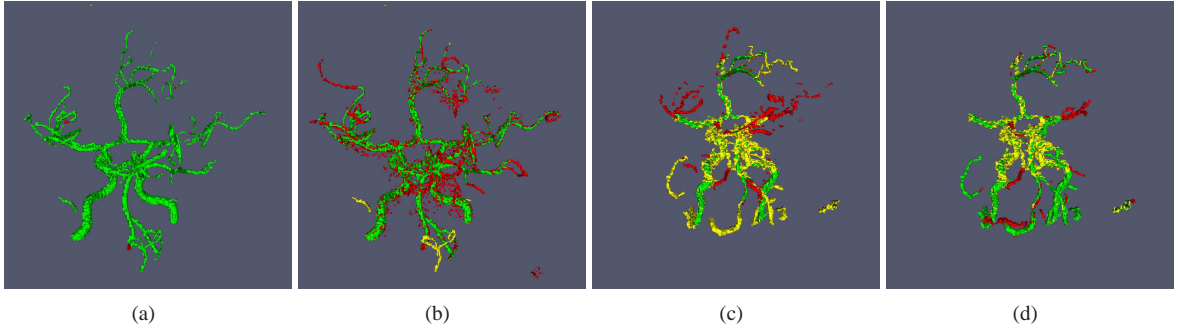


Figure 10: Segmentation results in an intra-patient case. In green: true positives. In yellow: false negatives. In red: false positives. (a) TOF MRA (TOF #1) segmentation using the TOF MRA ground-truth as example. (b) TOF MRA segmentation using the PC MRA ground-truth as example. (c) PC MRA (PC #1) segmentation using the TOF MRA ground-truth as example. (d) PC MRA segmentation using the PC MRA ground-truth as example.

6.2.2 Evaluation of the example quality

Secondly, we intend to evaluate the impact of the example quality on the segmentation accuracy, still without considering the effects of registration and of interpatient anatomical variability.

In order to do so, we consider two images of the same patient for which the segmentation ground-truth is available. One of these images is a (high resolution, high SNR) TOF MRA (TOF #1, considered above) thus associated to an accurate ground-truth. The other one is a (low resolution, low SNR) PC MRA (PC #1, considered above), associated with some less accurate ground-truth (which may be seen as a “blurred subset” of the TOF MRA ground-truth).

From these two images and associated ground-truths, we then perform four segmentations, which emphasize the behaviour of the segmentation method when applied on an accurate/non-accurate image with an accurate/non-accurate example.

As previously, the obtained results are expressed in terms of sensitivity and positive predictive value, gathered in Table 2. These results are also depicted in Figure 10. As mention above, the value of the standard measure are better in 1D than in 3D. These results emphasize the (expected) fact that the example has to present the same degree of details as the structures of interest to maximize the ability to correctly segment them. In case of heterogeneity between the example and the sought structures, an example of lower quality is less penalizing than an example of better quality, especially in terms of sensitivity.

6.2.3 Impact of the interpatient anatomical variability

We now intend to estimate the robustness of the segmentation method to vascular anatomical variations. These are generally high for vessels, by comparison to other (cerebral or non-cerebral) structures. Our experiments have been carried out from a quantitative point of view on the three same images as above, and from a qualitative point of view on a

Table 2: Sensitivity and positive predictive value measures for experiments of Section 6.2.2 (see text). The α value is the one for which the best segmentation has been obtained. The first and fourth lines correspond to the first and third lines of Table 1.

Image	Example	α	3D		1D	
			<i>Sen</i>	<i>PPV</i>	<i>Sen</i>	<i>PPV</i>
TOF #1	TOF #1	0.970	99.99	99.27	99.77	99.79
TOF #1	PC #1	0.855	92.48	86.46	93.72	92.13
PC #1	TOF #1	0.855	41.41	74.49	63.99	83.73
PC #1	PC #1	0.940	65.77	86.31	82.76	92.70

Table 3: Sensitivity and positive predictive value measures for experiments of Section 6.2.3 (see text). The α value is the one for which the best segmentation has been obtained. The best results are squared.

Example	Image	α	3D		1D	
			<i>Sen</i>	<i>PPV</i>	<i>Sen</i>	<i>PPV</i>
One image (case 1)	TOF #1	0.655	92.16	63.43	96.18	70.12
	TOF #2	0.870	76.87	75.31	93.35	90.09
	PC #1	0.740	43.28	61.96	66.23	72.93
One image (case 2)	TOF #1	0.630	93.85	63.95	94.85	70.56
	TOF #2	0.885	77.32	74.53	93.38	90.43
	PC #1	0.880	50.99	51.85	69.86	68.60
Mean image	TOF #1	0.680	93.67	74.25	95.02	80.63
	TOF #2	0.925	78.54	78.30	93.56	92.12
	PC #1	0.830	47.34	73.21	68.05	82.02

Table 4: Sensitivity and positive predictive value measures for experiments of Section 6.2.4 (see text). The α value is the one for which the best segmentation has been obtained. The best results are squared.

Registration	Image	α	3D		1D	
			<i>Sen</i>	<i>PPV</i>	<i>Sen</i>	<i>PPV</i>
Rigid	TOF #1	0.805	93.37	64.64	96.92	75.93
	TOF #2	0.855	89.00	86.04	97.50	94.68
	PC #1	0.935	49.05	65.24	69.38	76.48
Affine	TOF #1	0.680	90.17	77.77	94.58	81.77
	TOF #2	0.960	97.74	78.97	99.39	93.01
	PC #1	0.910	46.61	71.22	67.58	78.75
Nonrigid	TOF #1	0.680	93.67	74.25	95.02	80.63
	TOF #2	0.925	78.54	78.30	93.56	92.12
	PC #1	0.830	47.34	73.21	68.05	82.02

Table 5: Sensitivity and positive predictive value measures for experiments of Section 6.2.5 (see text). The α value is the one for which the best segmentation has been obtained. The best results are squared.

Connectivity	Image	α	3D		1D	
			<i>Sen</i>	<i>PPV</i>	<i>Sen</i>	<i>PPV</i>
6-	TOF #1	0.825	93.19	39.42	93.79	46.56
	TOF #2	0.970	92.60	38.83	94.44	68.90
26-	TOF #1	0.680	90.17	77.77	94.58	81.77
	TOF #2	0.960	97.74	78.97	99.39	93.01
Filter	TOF #1	0.895	87.54	60.35	84.18	76.35
	TOF #2	0.940	80.07	66.12	95.42	92.62

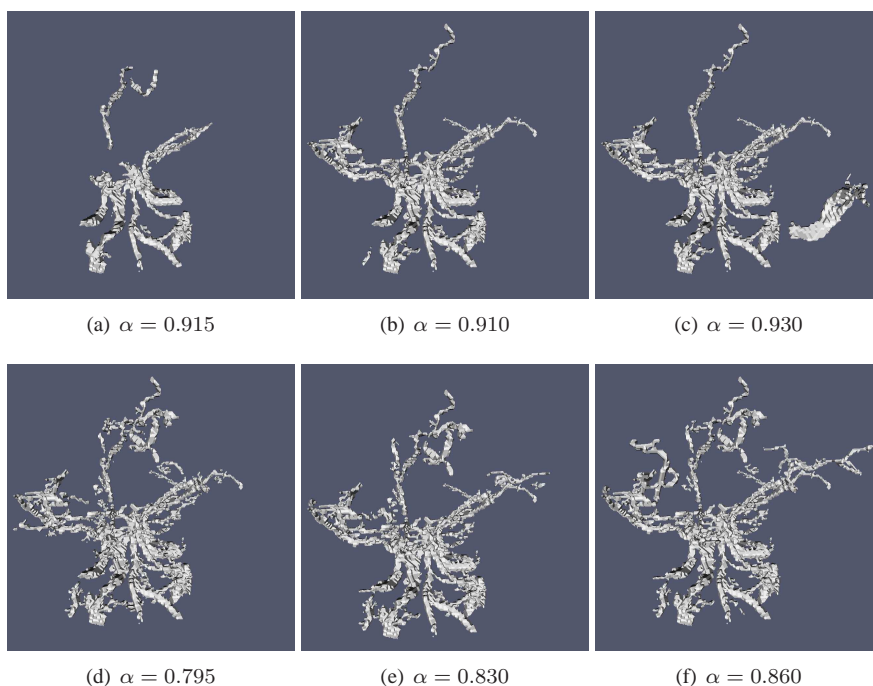


Figure 11: Segmentation results, on one of the 10 tested PC MRAs depending on the kind of example and the registration policy (see text). (a–c) Example consisting of one segmented image. (d–f) Example consisting of a mean image obtained from several segmented images. (a,d) Rigid registration. (b,e) Affine registration. (c,f) Nonrigid registration. The α value indicated for each subfigure is the one for which the best segmentation has been obtained.

dataset of 10 PC MRA images.

Experiments consist of performing segmentation with various examples, namely two examples obtained from two distinct PC MRA images (not considered for segmentation here), and a third example which is a “mean image” obtained from the preliminary segmentation of 20 PC MRA images (not considered for segmentation here). These examples are applied on the images to be segmented by performing nonrigid registration.

The obtained results for the first three images are gathered in Table 3. For the other 10 images, since no ground-truths are available, the validations have been made from a visual analysis (partially illustrated in Figure 11).

The first remark which can be made is related to the variability of the results with respect to the considered example, when such an example consists of one segmented image. Case 1 and Case 2, in Table 3, tend to suggest that the method is globally robust to the such example variability, in the case where the different examples are of similar accuracy, in particular for images of high resolution.

The second remark is related to the increase in quality induced by the use of an example consisting of a mean image of several segmented data. For such a mean example, the sensitivity measure is comparable to the case of single image examples, but the positive predictive value measure is significantly improved, both in terms of 3D and 1D results. This argues in favour of the use such mean examples, which are, in some ways, comparable to vascular atlases [11, 59], which better model the anatomical variability among a whole population.

6.2.4 Evaluation of the registration

The previous experiments have experimentally shown that the use of a mean image as example provides better results than the use of a single segmentation. In the further experiments, we then consider examples corresponding to such mean

images.

The purpose is here to evaluate the impact of the registration accuracy on the segmentation quality. By still considering the same datasets of 3 and 10 images as above, three segmentations are computed, by fitting the example thanks to a rigid, an affine, and a nonrigid registration procedure, respectively.

The obtained results for the first three images are gathered in Table 4. The results for the 10 images, still analysed in a visual fashion, are partially illustrated in Figure 11.

It appears that there is no clear correlation between the accuracy of the results and a specific registration policy. This probably denotes the limitations of the use of registration techniques mainly devoted to morphological structures. It emphasizes, in particular the actual need to propose vascular-oriented registration strategies, enabling to better take into account the specificities (sparseness, noise, etc.) of angiographic data, as already stated in Section 5.4.2.

6.2.5 Evaluation of the connectivity

In these last experiments, we finally assess the influence of the neighborhood connectivity on the quality of the segmentation results. In particular, we compare on the one hand the segmentation results obtained using the component-tree of an image I using the connectivity induced by the 6- and the 26-adjacencies, respectively; and on the other hand the ones obtained using the component-tree defined by the connectivity induced by the (extensive) mask $\mathcal{F}(I)$ of I , computed in the way described in Section 4.

These comparisons are performed on the two TOF MRAs (TOF #1 and TOF #2), by using the same mean image example as above. The segmentation results are depicted in Figure 12. Numerical results are given in Table 5.

From a quantitative point of view, the results are better in the case of the 26-adjacency. Nevertheless, from a visual inspection, we find the use of connectivity induced by the mask $\mathcal{F}(I)$ does allow some vessel reconnection. This fact does not appear in the numerical results, because of the difficulty to acquire correct ground-truth.

7 Conclusion

Two original methods have been proposed for 3D angiographic image filtering and segmentation. Both rely on recent advances in mathematical morphology. In particular, they take advantage of the mixture of discrete and continuous approaches (filtering method, Section 4.4.4), and of the low algorithmic cost of the involved strategies (filtering method–Proposition 4, and segmentation method–Proposition 7) leading to time-saving (fast, and automatic or interactive) image processing and analysis tools. It may be noticed that these two methods can be easily interfaced (Section 5.5) to directly integrate the filtering results in the segmentation process.

These methods have been validated on synthetic and real angiographic data, emphasizing their relevance. The ability to discriminate specific parts of the vascular structures (example-based approach) and to integrate the user’s skills with a low time cost has, in particular, led to use them in processes involving possibly large image datasets.

The following further works may also lead to improvements of these methods. Regarding vessel orientation computation (Section 4.4.2), the consideration of not only second-order derivatives, but also first-order ones may provide a better robustness to noise, and then improve vessel orientation estimates. Moreover, as for linear scale-space approach, a more elaborate analysis should be used, like automatic scale selection [39]. Finally, in terms of computation efficiency, the closed-form of Hessian matrix could be calculated [53] instead of the complete one. Regarding the morphological part of the filtering method, (Section 4.4.4), the size of the spatially-variant structuring elements could vary [18] according to the eigenvalues of the Hessian matrix. In addition, it is envisaged to use variable and more flexible structuring element shapes, such as paths instead of segments.

Regarding vessel segmentation (Section 5.4.3), instead of computing several segmentation results for different (chosen/sampled) α values, an alternative solution may be to provide the exhaustive (finite) set S of possible binary segmentations, modeled as a grey-level image $I_{out} : E \rightarrow [1, |S|]$. Such an approach –which may present a better time complexity than the current one– will be proposed soon.

Finally, vascular image registration (Section 5.4.2) also remains a challenging issue, in the case of the proposed image segmentation technique. The way to use not only morphological information from standard images, but also (sparse and

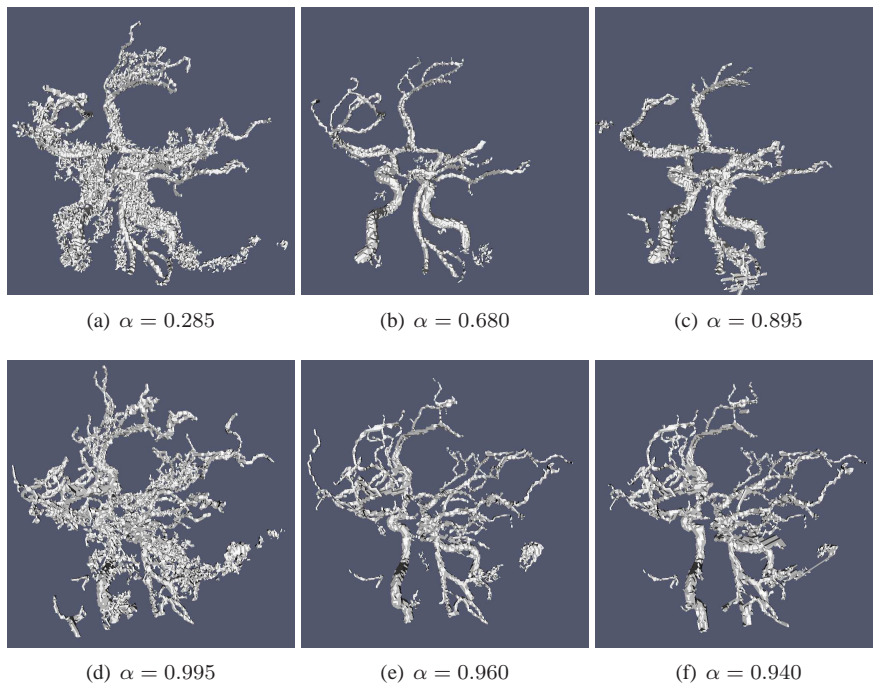


Figure 12: Segmentation results depending on the chosen connectivity (see text). Each column corresponds to a specific image (first row: TOF #1; second row: TOF #2). (a,d) Results for the 6-connectivity. (b,e) Results for the 26-connectivity. (c,f) Results for the connectivity induced by the filtering of Section 4. The α value indicated for each subfigure is the one for which the best segmentation has been obtained.

varying) vascular information from angiographic data, will also be considered in (longer term) further works, with the purpose of improving the accuracy of the example fitting.

Acknowledgements

The real angiographic data used for these experiments have been provided by the radiology service of the Civil Hospital, Strasbourg, France (PC MRA data), and the *In Vivo* Imaging Platform of Strasbourg University, Strasbourg, France (TOF MRA data).

The research leading to these results has been partially funded by a PhD grant of the *Région Alsace* and the *Centre National de la Recherche Scientifique* (CNRS), and has also received funding from the *Agence Nationale de la Recherche* (Grant Agreement ANR-2010-BLAN-0205).

References

- [1] Aylward, S.R., Bullitt, E., 2002. Initialization, noise, singularities, and scale in height ridge traversal for tubular object centerline extraction. *IEEE Transactions on Medical Imaging* 21, 61–75.
- [2] Aylward, S.R., Jomier, J., Weeks, S., Bullitt, E., 2003. Registration and analysis of vascular images. *International Journal of Computer Vision* 55, 123–138.

- [3] van Bemmél, C.M., Spreeuwers, L.J., Viergever, M.A., Niessen, W.J., 2003. Level-set-based artery-vein separation in blood pool agent CE-MR angiograms. *IEEE Transactions on Medical Imaging* 22, 1224–1234.
- [4] Bouaynaya, N., Charif-Chefchaoui, M., Schonfeld, D., 2008. Theoretical foundations of spatially-variant mathematical morphology part I: Binary images. *IEEE Transactions on Pattern Analysis and Machine Intelligence* 30, 823–836.
- [5] Bouaynaya, N., Schonfeld, D., 2008. Theoretical foundations of spatially-variant mathematical morphology part II: Gray-level images. *IEEE Transactions on Pattern Analysis and Machine Intelligence* 30, 837–850.
- [6] Bouraoui, B., Ronse, C., Baruthio, J., Passat, N., Germain, P., 2010. 3D segmentation of coronary arteries based on advanced Mathematical Morphology techniques. *Computerized Medical Imaging and Graphics* 34, 377–387.
- [7] Boykov, Y., Jolly, M., 2001. Interactive graph cuts for optimal boundary & region segmentation of objects in N-D images, in: *ICCV, Proceedings*, pp. 105–112.
- [8] Breen, E.J., Jones, R., 1996. Attribute openings, thinnings, and granulometries. *Computer Vision and Image Understanding* 64, 377–389.
- [9] Caldairou, C., Passat, N., Naegel, B., 2010. Attribute-filtering and knowledge extraction for vessel segmentation, in: *ISVC, Proceedings*, Springer. pp. 13–22.
- [10] Chen, J., Amini, A.A., 2004. Quantifying 3-D vascular structures in MRA images using hybrid PDE and geometric deformable models. *IEEE Transactions on Medical Imaging* 23, 1251–1262.
- [11] Chillet, D., Jomier, J., Cool, D., Aylward, S., 2003. Vascular atlas formation using a vessel-to-image affine registration method, in: *MICCAI, Proceedings*, Springer. pp. 335–342.
- [12] Chung, A.C.S., Noble, J.A., Summers, P.E., 2004. Vascular segmentation of phase contrast magnetic resonance angiograms based on statistical mixture modeling and local phase coherence. *IEEE Transactions on Medical Imaging* 23, 1490–1507.
- [13] Cline, H.E., Thedens, D.R., Meyer, C.H., Nishimura, D.G., Foo, T.K., Ludke, S., 2000. Combined connectivity and a gray-level morphological filter in magnetic resonance coronary angiography. *Magnetic Resonance in Medicine* 43, 892–895.
- [14] Cousty, J., Najman, L., Couprie, M., Clément-Guinaudeau, S., Goissen, T., Garot, J., 2010. Segmentation of 4D cardiac MRI: Automated method based on spatio-temporal watershed cuts. *Image and Vision Computing* 28, 1229–1243.
- [15] Descoteaux, M., Collins, D.L., Siddiqi, K., 2008. A geometric flow for segmenting vasculature in proton-density weighted MRI. *Medical Image Analysis* 12, 497–513.
- [16] Dogdas, B., Shattuck, D.W., Leahy, R.M., 2005. Segmentation of skull and scalp in 3-D human MRI using mathematical morphology. *Human Brain Mapping* 26, 273–285.
- [17] Dokládal, P., Bloch, I., Couprie, M., Ruijters, D., Urtasun, R., Garnero, L., 2003. Topologically controlled segmentation of 3D magnetic resonance images of the head by using morphological operators. *Pattern Recognition* 36, 2463–2478.
- [18] Dokládal, P., Dokládalová, E., 2008. Grey-scale morphology with spatially-variant rectangles in linear time, in: *ACIVS, Proceedings*, Springer. pp. 674–685.
- [19] Dufour, A., Passat, N., Naegel, B., Baruthio, J., 2011. Interactive 3D brain vessel segmentation from an example, in: *ISBI, Proceedings*, pp. 1121–1124.

- [20] Eichel, P.H., Delp, E.J., Koral, K., Buda, A.J., 1988. A method for a fully automatic definition of coronary arterial edges from cineangiograms. *IEEE Transactions on Medical Imaging* 7, 313–320.
- [21] Faisan, S., Passat, N., Noblet, V., Chabrier, R., Meyer, C., In press. Topology-preserving warping of binary images according to one-to-one mappings. *IEEE Transactions on Image Processing*.
- [22] Flasque, N., Desvignes, M., Constans, J.M., Revenu, M., 2001. Acquisition, segmentation and tracking of the cerebral vascular tree on 3D magnetic resonance angiography images. *Medical Image Analysis* 5, 173–183.
- [23] Frangi, A.F., Niessen, W.J., Hoogeveen, R.M., van Walsum, T., Viergever, M.A., 1999. Model-based quantitation of 3-D magnetic resonance angiographic images. *IEEE Transactions on Medical Imaging* 18, 946–956.
- [24] Friman, O., Hindennach, M., Kühnel, C., Peitgen, H.O., 2009. Multiple hypothesis template tracking of small 3D vessel structures. *Medical Image Analysis* 14, 160–171.
- [25] Gui, L., Lisowski, R., Faundez, T., Huppi, P.S., Lazeyras, F., Kocher, M., 2011. Automatic segmentation of newborn brain MRI using mathematical morphology, in: *ISBI, Proceedings*, pp. 2026–2030.
- [26] Heijmans, H., 1991. Theoretical aspects of gray-level morphology. *IEEE Transactions on Pattern Analysis and Machine Intelligence* 13, 568–582.
- [27] Hernandez, M., Frangi, A.F., 2007. Non-parametric geodesic active regions: Method and evaluation for cerebral aneurysms segmentation in 3DRA and CTA. *Medical Image Analysis* 11, 224–241.
- [28] Holden, M., 2008. A review of geometric transformations for nonrigid body registration. *IEEE Transactions on Medical Imaging* 27, 111–128.
- [29] Jomier, J., Aylward, S.R., 2004. Rigid and deformable vasculature-to-image registration: A hierarchical approach, in: *MICCAI, Proceedings, Springer*. pp. 829–836.
- [30] Jones, R., 1999. Connected filtering and segmentation using component trees. *Computer Vision and Image Understanding* 75, 215–228.
- [31] Kitamura, K., Tobis, J.M., Sklansky, J., 1988. Estimating the 3D skeletons and transverse areas of coronary arteries from biplane angiograms. *IEEE Transactions on Medical Imaging* 7, 173–187.
- [32] Kobashi, S., Kamiura, N., Hata, Y., Miyawaki, F., 2001. Volume-quantization-based neural network approach to 3D MR angiography image segmentation. *Image and Vision Computing* 19, 185–193.
- [33] Kong, T.Y., Rosenfeld, A., 1989. Digital topology: Introduction and survey. *Computer Vision, Graphics, and Image Processing* 48, 357–393.
- [34] Krissian, K., Malandain, G., Ayache, N., Vaillant, R., Troussset, Y., 2000. Model-based detection of tubular structures in 3D images. *Computer Vision and Image Understanding* 80, 130–171.
- [35] Lesage, D., Angelini, E.D., Bloch, I., Funka-Lea, G., 2009a. Design and study of flux-based features for 3D vascular tracking, in: *ISBI, Proceedings*, pp. 286–289.
- [36] Lesage, D., Angelini, E.D., Bloch, I., Funka-Lea, G., 2009b. A review of 3D vessel lumen segmentation techniques: Models, features and extraction schemes. *Medical Image Analysis* 13, 819–845.
- [37] Li, H., Yezzi, A.J., 2007. Vessels as 4-D curves: Global minimal 4-D paths to extract 3-D tubular surfaces and centerlines. *IEEE Transactions on Medical Imaging* 26, 1213–1223.
- [38] Lindeberg, T., 1994. *Scale-Space Theory in Computer Vision*. Kluwer Academic Publishers.

- [39] Lindeberg, T., 1998. Feature detection with automatic scale selection. *International Journal of Computer Vision* 30, 79–116.
- [40] Lorenz, C., Carlsen, I.C., Buzug, T.M., Fassnacht, C., Weese, J., 1997. Multi-scale line segmentation with automatic estimation of width, contrast and tangential direction in 2D and 3D medical images, in: *CVRMed-MRCAS, Proceedings*, Springer. pp. 233–242.
- [41] Lorigo, L.M., Faugeras, O.D., Grimson, W.E.L., Keriven, R., Kikinis, R., Nabavi, A., Westin, C.F., 2001. CURVES: Curve evolution for vessel segmentation. *Medical Image Analysis* 5, 195–206.
- [42] Manniesing, R., Viergever, M.A., Niessen, W.J., 2006. Vessel enhancing diffusion: A scale space representation of vessel structures. *Medical Image Analysis* 10, 815–825.
- [43] Manniesing, R., Viergever, M.A., Niessen, W.J., 2007. Vessel axis tracking using topology constrained surface evolution. *IEEE Transactions on Medical Imaging* 26, 309–316.
- [44] Maragos, P., Vachier, C., 2009. Overview of adaptive morphology: Trends and perspectives, in: *ICIP, Proceedings*, pp. 2241–2244.
- [45] McGuinness, K., O’Connor, N.E., 2010. A comparative evaluation of interactive segmentation algorithms. *Pattern Recognition* 43, 434–444.
- [46] Naegel, B., 2007. Using mathematical morphology for the anatomical labeling of vertebrae from 3D CT-scan images. *Computerized Medical Imaging and Graphics* 31, 141–156.
- [47] Naegel, B., Passat, N., Boch, N., Kocher, M., 2007a. Segmentation using vector-attribute filters: methodology and application to dermatological imaging, in: *ISMM, Proceedings, INPE*. pp. 239–250.
- [48] Naegel, B., Passat, N., Ronse, C., 2007b. Grey-level hit-or-miss transforms—Part I: Unified theory. *Pattern Recognition* 40, 635–647.
- [49] Naegel, B., Passat, N., Ronse, C., 2007c. Grey-level hit-or-miss transforms—Part II: Application to angiographic image processing. *Pattern Recognition* 40, 648–658.
- [50] Najman, L., Couprie, M., 2006. Building the component tree in quasi-linear time. *IEEE Transactions on Image Processing* 15, 3531–3539.
- [51] Najman, L., Talbot, H. (Eds.), 2010. *Mathematical morphology: from theory to applications*. ISTE/J. Wiley & Sons.
- [52] Noblet, V., Heinrich, C., Heitz, F., Armspach, J.P., 2005. 3-D deformable image registration: a topology preservation scheme based on hierarchical deformation models and interval analysis optimization. *IEEE Transactions on Image Processing* 14, 553–566.
- [53] Orłowski, P., Orkisz, M., 2009. Efficient computation of Hessian-based enhancement filters for tubular structures in 3D images. *IRBM* 30, 128–132.
- [54] Ouzounis, G.K., Wilkinson, M.H.F., 2007. Mask-based second-generation connectivity and attribute filters. *IEEE Transactions on Pattern Analysis and Machine Intelligence* 29, 990–1004.
- [55] Passat, N., Naegel, B., 2011a. Component-hypertrees for image segmentation, in: *ISMM, Proceedings, Springer*. pp. 284–295.
- [56] Passat, N., Naegel, B., 2011b. Selection of relevant nodes from component-trees in linear time, in: *DGCI, Proceedings, Springer*. pp. 453–464.
- [57] Passat, N., Naegel, B., Rousseau, F., Koob, M., Dietemann, J.L., 2011. Interactive segmentation based on component-trees. *Pattern Recognition* 44, 2539–2554.

- [58] Passat, N., Ronse, C., Baruthio, J., Armspach, J.P., Foucher, J., 2007. Watershed and multimodal data for vessel segmentation: Application to the superior sagittal sinus. *Image and Vision Computing* 25, 512–521.
- [59] Passat, N., Ronse, C., Baruthio, J., Armspach, J.P., Maillot, C., 2006. Magnetic resonance angiography: From anatomical knowledge modeling to vessel segmentation. *Medical Image Analysis* 10, 259–274.
- [60] Passat, N., Ronse, C., Baruthio, J., Armspach, J.P., Maillot, C., Jahn, C., 2005. Region-growing segmentation of brain vessels: An atlas-based automatic approach. *Journal of Magnetic Resonance Imaging* 21, 715–725.
- [61] Ronse, C., 1998. Set-theoretical algebraic approaches to connectivity in continuous or digital spaces. *Journal of Mathematical Imaging and Vision* 8, 41–58.
- [62] Sabry Hassouna, M., Farag, A.A., Hushek, S., Moriarty, T., 2006. Cerebrovascular segmentation from TOF using stochastic models. *Medical Image Analysis* 10, 2–18.
- [63] Salembier, P., Garrido, L., 2000. Binary partition tree as an efficient representation for image processing, segmentation and information retrieval. *IEEE Transactions on Image Processing* 9, 561–576.
- [64] Salembier, P., Oliveras, A., Garrido, L., 1998. Anti-extensive connected operators for image and sequence processing. *IEEE Transactions on Image Processing* 7, 555–570.
- [65] Salembier, P., Wilkinson, M.H.F., 2009. Connected operators: A review of region-based morphological image processing techniques. *IEEE Signal Processing Magazine* 26, 136–157.
- [66] Sato, Y., Nakajima, S., Shiraga, N., Atsumi, H., Yoshida, S., Koller, T., Gerig, G., Kikinis, R., 1998. Three-dimensional multi-scale line filter for segmentation and visualization of curvilinear structures in medical images. *Medical Image Analysis* 2, 143–168.
- [67] Serra, J., 1998. Connectivity on complete lattices. *Journal of Mathematical Imaging and Vision* 9, 231–251.
- [68] Suh, J.W., Scheinost, D., Qian, X., Sinusas, A.J., Breuer, C.K., Papademetris, X., 2010. Serial non rigid vascular registration using weighted normalized mutual information, in: *ISBI, Proceedings*, pp. 25–28.
- [69] Sun, K.Q., Sang, N., 2008. Morphological enhancement of vascular angiogram with multiscale detected by Gabor filters. *Electronics Letters* 44, 86–87.
- [70] Tankyevych, O., Talbot, H., Dokládál, P., Passat, N., 2009a. Direction-adaptive grey-level morphology. Application to 3D vascular brain imaging, in: *ICIP, Proceedings*, pp. 2261–2264.
- [71] Tankyevych, O., Talbot, H., Dokládál, P., Passat, N., 2009b. Spatially variant morpho-Hessian filter: efficient implementation and application, in: *ISMM, Proceedings*, Springer. pp. 137–148.
- [72] Tankyevych, O., Talbot, H., Passat, N., Musacchio, M., Lagneau, M., 2011. Angiographic image analysis., in: Dougherty, G. (Ed.), *Medical Image Processing: Techniques and Applications*. Springer. chapter 5.
- [73] Thackray, B.D., Nelson, A.C., 1993. Semi-automatic segmentation of vascular network images using a rotating structuring element (ROSE) with mathematical morphology and dual feature thresholding. *IEEE Transactions on Medical Imaging* 12, 385–392.
- [74] Tizon, X., Smedby, Ö., 2002. Segmentation with gray-scale connectedness can separate arteries and veins in MRA. *Journal of Magnetic Resonance Imaging* 15, 438–445.
- [75] Urbach, E.R., Boersma, N.J., Wilkinson, M.H.F., 2005. Vector attribute filters, in: *ISMM, Proceedings*, Springer SBM. pp. 95–104.
- [76] Urbach, E.R., Wilkinson, M.H.F., 2002. Shape-only granulometries and gray-scale shape filters, in: *ISMM, Proceedings*, CSIRO Publishing. pp. 305–314.

- [77] Verdú-Monedero, R., Angulo, J., 2008. Spatially-variant directional mathematical morphology operators based on a diffused average squared gradient field, in: ACIVS, Proceedings, Springer. pp. 542–553.
- [78] Vincent, L., Soille, P., 1991. Watersheds in digital spaces: an efficient algorithm based on immersion simulations. *IEEE Transactions on Pattern Analysis and Machine Intelligence* 13, 583–598.
- [79] Wilkinson, M.H.F., Gao, H., Hesselink, W.H., Jonker, J.E., Meijster, A., 2008. Concurrent computation of attribute filters on shared memory parallel machines. *IEEE Transactions on Pattern Analysis and Machine Intelligence* 30, 1800–1813.
- [80] Wilkinson, M.H.F., Westenberg, M.A., 2001. Shape preserving filament enhancement filtering, in: MICCAI, Proceedings, Springer. pp. 770–777.
- [81] Wong, W.C.K., Chung, A.C.S., 2007. Probabilistic vessel axis tracing and its application to vessel segmentation with stream surfaces and minimum cost paths. *Medical Image Analysis* 11, 567–587.
- [82] Xu, C., Prince, J.L., 1998. Snakes, shapes, and gradient vector flow. *IEEE Transactions on Image Processing* 7, 359–369.
- [83] Zana, F., Klein, J.C., 2001. Segmentation of vessel-like patterns using mathematical morphology and curvature evaluation. *IEEE Transactions on Image Processing* 10, 1010–1019.